

Copyright
By
Travis Bertram Richards
2005

**Weathering Steel for Maglev Guideway Construction:
Preliminary Temperature Analysis**

by

Travis Bertram Richards, B.S.

Thesis

Presented to the Faculty of the Graduate School of
The University of Texas at Austin
in Partial Fulfillment
of the Requirements
for the Degree of

Master of Science in Engineering

The University of Texas at Austin

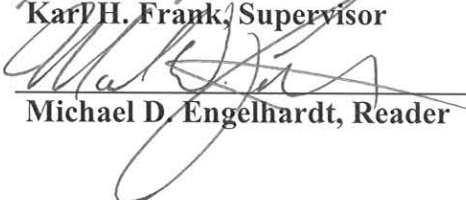
May 2005

**Weathering Steel for Maglev Guideway Construction:
Preliminary Temperature Analysis**

**APPROVED BY
SUPERVISING COMMITTEE:**



Karl H. Frank, Supervisor



Michael D. Engelhardt, Reader

Dedication

To my parents, who offer me love and support and to my sister, who makes me laugh.

Acknowledgements

I would like to thank Dr. Karl Frank for all of his help and guidance throughout the duration of this project. If it were not for his sincere commitment to his students, this research and report would not have been possible. I thank Dr. Michael Engelhardt for his helpful comments and his contribution to the quality of this report. I thank Hyeong Jun Kim for the opportunity to absorb his knowledge of heat transfer principles as well as Kyle Riding and Jason Ideker for going out of their way to provide a significant portion of the weather data referenced in this report. I wish Hyeong, Kyle and Jason the best of luck with their dissertations. I thank the laboratory and administrative staff at Ferguson Lab for being smiling faces and for facilitating an important part of the education received from the Structural Engineering program at The University of Texas at Austin. In particular, I would like to thank Mike Wason for showing me how to make thermocouples. I would also like to thank Dr. John Breen for giving me the opportunity to receive an education from such a fine institution. Lastly, I thank my family and close friends for supporting me throughout my academic endeavors. In particular, I thank Melissa for not only reading this report, but for inspiring me over the past six years to spend just that one more minute to make that homework, group project, or thesis better than it was before.

May 6, 2005

Weathering Steel for Maglev Guideway Construction:
Preliminary Temperature Analysis

Travis Bertram Richards, M.S.E.

The University of Texas at Austin, 2005

SUPERVISOR: Karl H. Frank

This study investigates the possibility of using weathering steel to construct a guideway for a magnetically levitated train. The thermal behavior of weathering steel is compared to that of steel plates with other coatings and the temperature gradients monitored on a full-size weathered girder are analyzed. The findings of this report indicate that a guideway constructed of weathering steel will have a thermal behavior similar that of a blackbody and may experience large temperature gradients under certain weather conditions. Some of the material properties needed to use a finite element program to predict the temperature deflections of a weathering steel guideway are also described.

Table of Contents

Table of Contents	vii
List of Tables.....	x
List of Figures	xi
CHAPTER 1 INTRODUCTION.....	1
1.1 Faster Travel Alternative.....	1
1.2 Scope and Objectives of Research	1
1.3 Scope of This Report.....	2
CHAPTER 2 BACKGROUND INFORMATION.....	4
2.1 Maglev Technology.....	4
2.2 Advantages of the Maglev Train.....	4
2.3 Guideway Design	5
2.4 Deflection Limits.....	5
2.5 Temperature Loading – Previous Research on Maglev	6
2.6 Heat Transfer.....	8
2.7 Temperature Related Work on Bridges in The United States	10
CHAPTER 3 MATERIAL PROPERTIES	11
3.1 Weathering Steel	11
3.2 Instrumentation.....	12
3.2.1 Thermocouples	12
3.2.2 Pyranometers.....	13
3.2.3 Datalogger	14

3.2.4 Additional Weather Stations	15
3.3 Preparation of Steel Plates With Different Surface Conditions	15
3.4 Calibration	17
3.5 Effect of Surface Conditions	17
3.6 Effect of Steel Area and Geometry	20
3.7 Solar Reflectivity.....	23
3.8 Emissivity	29
3.9 Convection Coefficient	30
3.10 Conclusions	35
CHAPTER 4 GIRDER PROPERTIES	37
4.1 Description and Location of Girder	37
4.2 Experiment Setup	39
4.3 Vertical Temperature Gradient.....	41
4.4 Lateral Temperature Gradient	46
4.5 Temperature Variation Along Girder.....	52
4.6 Conclusions	57
CHAPTER 5 FLAT PLATE TEMPERATURE PREDICTIONS	59
5.1 Introduction	59
5.2 Temperature Change Over Time.....	59
5.3 Prediction Methods	60
5.3.1 Convection Coefficient	61
5.3.2 Time Step for Experimental Data.....	62

5.4 Updated Prediction Method	67
5.4.1 Effective Sky Temperature.....	68
5.4.2 Linear Calculation of Convection Coefficient	68
5.5 Results and Conclusions.....	70
CHAPTER 6 CONCLUSIONS.....	73
6.1 Temperature Measurements and Thermal Gradients	73
6.2 Implementation of Maglev Technology	75
APPENDIX	76
REFERENCES	82
VITA	84

List of Tables

Table 3.1 Summary of Steel Plates	16
Table 3.2 Order for Reflectivity Experiment (October 14 2004).....	26
Table 4.1 Comparison of Weather Conditions (KATT Weather Station).....	48
Table 4.2 Comparison of Temperature Gradients Measurements.....	56
Table 5.1 Maximum Errors for One-Hour Interval Weather Data.....	67
Table 5.2 Maximum Errors for Ten-Minute Interval Weather Data.....	67
Table 5.3 Maximum Errors from Predictions Using Program	69

List of Figures

Figure 2.1 Depiction of System Developed by TRI (Henke and Falkner).....	5
Figure 2.2 Examples of Heat Transfer Components (Mangerig et al., 2003)	7
Figure 3.1 Pyranometers: LI200X and CM3 (CSI 1997 and CSI 2002).....	14
Figure 3.2 Photograph of 21X Micrologger.....	14
Figure 3.3 Cross Section of Test Plates.....	16
Figure 3.4 Photograph of Plate Stand.....	18
Figure 3.5 Solar Radiation & Temperature vs. Time (July 9-12 2004)	19
Figure 3.6 Temp vs. Time for Different Surface Conditions (July 10 2004).....	20
Figure 3.7 Test Setup for Plate Temperature Measurements	21
Figure 3.8 Solar Radiation & Temperature vs. Time (September 17 2004)	22
Figure 3.9 Bottom Coating - Temperature vs. Time (September 17 2004)	22
Figure 3.10 Plates & Girder – Solar Radiation & Temp vs. Time (Sept 17 2004)23	
Figure 3.11 Solar Reflectivity Experiment Setup	24
Figure 3.12 Movement of Plates underneath Pyranometer - Plan View	25
Figure 3.13 Solar Reflectivity vs. Time (October 14 2004).....	28
Figure 3.14 Plate Positions for Reflectivity Experiment.....	29
Figure 3.15 Photograph of Test Plates Hanging After Being Heated in an Oven.31	
Figure 3.16 Comparison of Cooling Curves for Three Plates (Nov 12 2004)	33
Figure 3.17 Temperature vs. Time – Forced Convection (November 12 2004) ...	34
Figure 3.18 Temperature vs. Time – Natural Convection (November 12 2004) ..	35
Figure 4.1 Cross Section of Full Size Girder	38
Figure 4.2 Map of Girder Location	38
Figure 4.3 Test Setup for Thermal Gradient Measurements	40
Figure 4.4 Attachment of Thermocouple to Girder Surface	41
Figure 4.5 Solar Radiation & Temp vs. Time (December 11-12 2004).....	42
Figure 4.6 Flange Temperatures vs. Time (December 11-12 2004)	43

Figure 4.7 Girder Cross Section at Maximum Vertical Temperature Gradient	45
Figure 4.8 Solar Radiation & Temp vs. Time (November 25-26 2004)	46
Figure 4.9 Web Temperatures vs. Time (November 25-26 2004)	49
Figure 4.10 Comparison of Web and Flange Temps vs. Time (Nov 25-26 2004)	49
Figure 4.11 Girder Cross Section at Maximum Lateral Temperature Gradient....	51
Figure 4.12 Photograph of Morning Sunlight Hitting Eastern Web	52
Figure 4.13 Solar Radiation and Temp vs. Time (December 7 2004)	53
Figure 4.14 Temp vs. Length – Heating of West Web, Top 1/4 Pt. (Dec 7 2004)	54
Figure 4.15 Temp vs. Length – Heating of East Web, Top 1/4 Pt. (Dec 7 2004).	55
Figure 4.16 Temp vs. Girder Length – West Web – Afternoon (Dec 7 2004).....	56
Figure 4.17 Temp vs. Girder Length – East Web – Afternoon (Dec 7 2004).....	56
Figure 4.18 Vertical & Lateral Temp Gradients along Girder (Dec 7 2004).....	57
Figure 5.1 Comparison of Prediction Methods (July 31 2004).....	64
Figure 5.2 Breakdown of Prediction Contributions (July 31 2004).....	65
Figure 5.3 Weather Conditions (July 31 2004).....	66
Figure 5.4 Comparison of Predicted & Measured Temps (September 13 2004) ..	71

CHAPTER 1

Introduction

1.1 FASTER TRAVEL ALTERNATIVE

Using a magnetic field to lift and propel a train was based on the idea of reaching high traveling speeds by eliminating friction between the train and its track. Transrapid International (TRI) developed a magnetically levitated (Maglev) train system and after twenty years of empirical work at the test track in Emsland, Germany has produced a train capable of traveling at speeds of 500 km/h. Since this is significantly faster than any current ground transportation available in the United States, a Maglev train could provide a viable alternative for travelers over moderate distances. The environmental advantage of low emissions provides an additional benefit.

1.2 SCOPE AND OBJECTIVES OF RESEARCH

The current research at the Ferguson Structural Engineering Laboratory (FSEL) is part of the initial work to accomplish the larger goal of constructing and operating a Maglev track in the United States. Constructing a Maglev system using the German technology involves designing a guideway for the train that meets the stringent specifications of Transrapid. This design process involves fabricating and installing a segment of the guideway design in the test track in Germany to evaluate its performance. Upon confirmation that the design is satisfactory, a 40-mile track may be constructed at one of the proposed American routes for an initial Maglev line.

The deflection limits set by TRI are more stringent than what is typical in the United States for bridges and buildings. For example, the deflection limit is

L/4000 for a single span member under vehicle load (TRI 2002). Since a high level of accuracy is desired for the deflection and stress calculations, the design analysis will be performed using a finite element program (ABAQUS). The finite element model used will be described in the future dissertation of Hyeong Jun Kim, a doctoral student at The University of Texas at Austin.

1.3 SCOPE OF THIS REPORT

Although a Maglev guideway could be constructed using different materials, the research in this report focused on the potential of constructing a guideway using weathering steel. Weathering steel refers to steel types that develop a dense oxide layer at the surface that protects against long-term corrosion (Albrecht and Naeemi 1984).

Due to the extreme deflection criterion, L/8000 for thermal loading, temperature related curvatures are more of a concern for a Maglev guideway than for other structures. Research regarding climate-induced deformations on the Transrapid system showed that using highly reflective paints reduced temperature deflections (Mangerig et al., 2003). Although Mangerig's research suggested that steel guideways with untreated surfaces violated the thermal deflection limit on most days, this project focused on gaining a better understanding of the behavior of weathering steel in extreme climate conditions. Weathering steel is being investigated because it eliminates the maintenance costs and service interruptions associated with painting the guideway. Reducing the cost of the guideway would make the Maglev system a more attractive high-speed system.

The temperatures of small steel plates, representing the surfaces of guideway members, were monitored while the plates were exposed to the climate in Austin, Texas. These tests were performed on plates with three coatings: weathering, ultra flat black paint, and bright silver paint, to determine how the

behavior of the weathered steel plate compared to that of a blackbody and a bright colored plate. To approximate the surface of weathering steel, steel plates that developed an oxide layer due to normal atmospheric conditions, or weathered, were used. Additional tests were performed on a weathered surface to determine the properties needed to predict the thermal response of the plate to meteorological conditions.

Verifying the prediction method for the small plates would allow the same method to be used in combination with ABAQUS to predict the thermal behavior of a girder that was monitored during this project. Temperature measurements were taken over the cross section of a full size weathered tub girder to provide data to which the predictions could be compared and to determine typical temperature gradient magnitudes and the conditions under which they occurred. Applying this information to accurately predict the temperature gradients for the American guideway design would determine the feasibility of constructing a guideway using weathering steel. In addition to describing the temperature monitoring of the small steel plates and the full size girder, this report describes the initial predictions of the thermal behavior of the plates and provides the material properties of weathered steel needed to perform predictions using a finite element program.

CHAPTER 2

Background Information

2.1 MAGLEV TECHNOLOGY

The technology for the high-speed magnetically levitated (Maglev) train was developed in order to eliminate the contact between a train and its track, and thus the friction force the train experiences. By eliminating the friction force, higher traveling speeds are suddenly possible. The train developed by Transrapid International in Germany is propelled by a long-stator linear motor, which is laid out along the length of the track (Henke and Falkner). This linear magnet creates an electromagnetic traveling field that levitates the train 10 mm above the track and propels it in the desired direction of travel. To decrease the speed of the train without the help of the friction force, the direction of the traveling electromagnetic field is reversed. A sketch of the system used to propel the train is shown in Figure 2.1.

2.2 ADVANTAGES OF THE MAGLEV TRAIN

The first commercially operational Maglev train using Transrapid's technology was completed in Shanghai, China in 2002. The train, which runs on a concrete guideway, has reached speeds up to 501 km/h with passengers on board. This is significantly higher than the operating speeds of 300 km/h achieved by the fastest modern railway systems in Germany, France, and Japan. In addition to the most apparent advantage of increased speed, Transrapid International states that the Maglev train technology, when compared to the German Intercity Express (ICE) 3, provides a transportation system that requires less energy consumption, produces lower noise emissions, makes less of an

environmental impact, requires less space, and provides a safer and more comfortable ride to its passengers (TRI 2003).

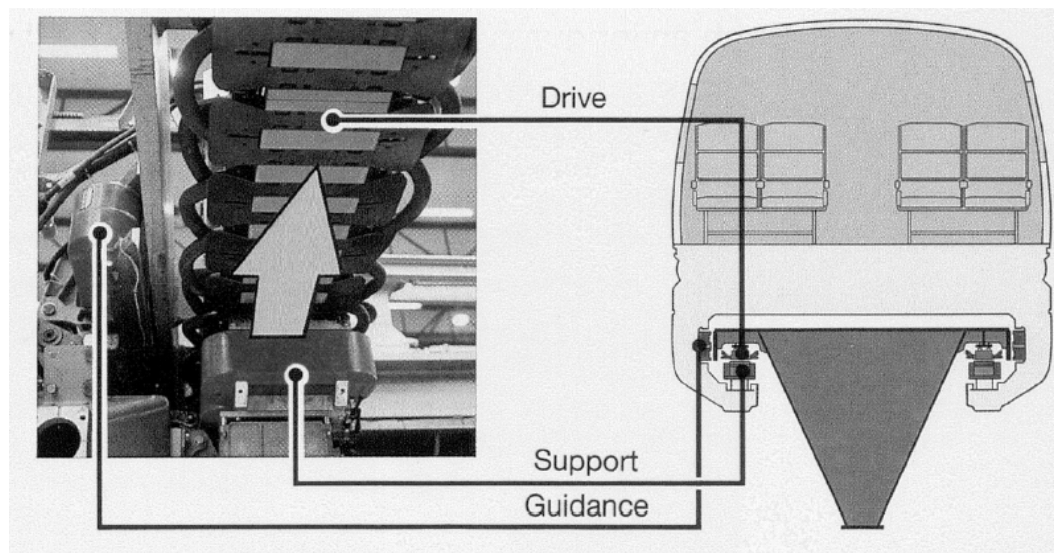


Figure 2.1 Depiction of System Developed by TRI (Henke and Falkner)

2.3 GUIDEWAY DESIGN

In order to use the technology developed by Transrapid International to construct a Maglev train system, the interested owner must provide TRI with a track, or guideway design. This design must satisfy both the local transportation codes of the project site and the stringent experimentally based requirements established by Transrapid. The load cases presented by TRI, including forces due to the train on the guideway, must be considered along with local conditions, such as wind and/or earthquakes, to determine the governing load combination. Thermal loading is one of the forces that must be defined for the project site.

2.4 DEFLECTION LIMITS

Since the separation between the train and guideway during levitation is small, the deflection limits specified by Transrapid are more stringent than what is

typically seen in practice. The deflection limit for a single span guideway under vehicle load is $L/4000$, or 7.8 mm for a 31 m span (TRI 2002). For a double span guideway, the deflection limit under the same loading is $L/4800$, or 6.5 mm for a 31 m span. The allowable vertical deflection due to a temperature gradient is $L/8000$.

2.5 TEMPERATURE LOADING – PREVIOUS RESEARCH ON MAGLEV

In order to satisfy temperature deflection limits, design temperature gradients in both the vertical and lateral directions over a guideway cross section are determined for each project site. Exceeding these gradients can cause the temperature deflections that TRI wants to avoid. In particular, vertical temperature gradients and deflection limits are intended to minimize the angle of rotation at the ends of the beams. The maximum allowable angle is specified as 6.2×10^{-4} and 7.4×10^{-4} radians for upward and downward thermal deflections, respectively (Mangerig et al., 2003). If the limits are violated, scheduling delays may occur due to reduced speeds.

Temperature related research was performed on Transrapid guideways for over a decade in order to determine how often deflection limits were violated under temperature loading and to explore design alternatives that could minimize the need for additional materials and funds. This research involved measuring the temperature variation over the cross section of different guideway types and determining the resulting deflections. It also involved using regional climate data over an extended period of time to develop a simulation software tool that could model the heat transfer modes shown in Figure 2.2 for various material properties. Tests using meteorological data from 1997 to 2000 showed a good correlation between the extreme temperature values determined using long-term simulations and those that were measured (Mangerig et al., 2003). The results of this testing

showed that although dead and live load limits were satisfied, the temperature deflection criteria was violated on at least a few days for all of the existing guideway designs.

A comparison of an untreated steel surface and a white painted guideway was also performed. This comparison showed that the untreated steel girder failed to satisfy the deflection limits on most days. While the reflective paint noticeably decreased the frequency of the deflection criteria violations, on days when the deflections were above the allowable limit, they were significantly above.

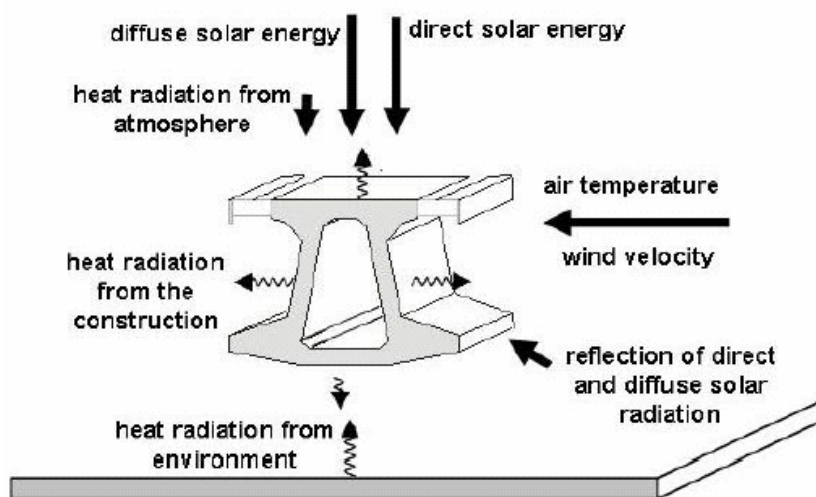


Figure 2.2 Examples of Heat Transfer Components (Mangerig et al., 2003)

Despite the reduction in the number of days that the thermal deflection limit was exceeded, the costs associated with cleaning and repainting the guideway make using highly reflective paint a less desirable solution. The increase in cost and service delays due to maintenance motivated Transrapid to look at structural design alternatives to alleviate the temperature deflection

problem. These design improvements were intended to minimize the temperature gradient over the section.

The design alternatives included widening the bottom flange of the guideway to expose its ends to the same solar radiation as the top flange (Mangerig et al., 2003). Adjustments to the camber of the guideway and placing a short guideway section at each column support to separate the angled ends of adjacent longer beams were also suggested to minimize the effects of thermal deflections. Additional research indicated that using a double-span guideway produced 30% lower vertical thermal deformations than a single-span beam (Henke and Falkner). The decision over which of these options would be the most economical, depending on material, maintenance, shipping, and labor costs, would be made after receiving input from guideway manufacturers (Mangerig et al., 2003).

2.6 HEAT TRANSFER

Heat transfer is the movement of energy that will cause a change in temperature (Incropera and DeWitt 2002). The process of heat transfer consists of the three modes of conduction, convection, and radiation. Some of the components of these modes experienced by a Maglev guideway are shown in Figure 2.2. The conduction mode refers to the transfer of heat through the random interaction of particles in a stationary medium. When a temperature gradient exists, conduction occurs in the direction of the cooler, less energetic particles.

Convection also consists of the interaction of particles, but in combination with the motion of a fluid (Incropera and DeWitt 2002). Convection is often categorized as either forced or natural. Forced convection refers to airflow that is caused by a fan, pump, or atmospheric winds. Natural convection refers to flow

caused by a difference in temperature between a surface and the fluid molecules adjacent to the surface. This temperature difference causes heat transfer through conduction and results in a density gradient in the fluid molecules in the boundary layer. This gradient causes a buoyancy force, which in turn produces fluid motion past the surface.

In actual conditions, the convection mode typically involves a combination of natural and forced airflow. The efficiency of this mode of heat transfer is dependent on the convection coefficient of a surface. This coefficient is affected by the type of fluid moving past the surface, the flow condition, the flow rate, and the surface geometry. The more turbulent the air flow, the higher the convection coefficient and the more vigorous the heat transfer.

The radiation mode of heat transfer occurs due to matter with a nonzero temperature emitting electromagnetic waves (Incropera and DeWitt 2002). Even in a vacuum, heat transfer occurs through thermal radiation in the presence of a temperature gradient. If two objects are in thermal equilibrium, no radiation heat transfer will occur. The emissivity of the object's surface determines the percentage of the radiation the object emits at a given temperature, relative to the emission of a blackbody. Irradiation refers to radiation produced from an object's surroundings, including the sun, to which an object is exposed. The object's surface and the irradiation type determine the percentage of the irradiation that contributes to heat transfer, or the absorptivity.

The earth's surface is exposed to radiation emitted by the atmosphere and the sun. The atmospheric radiation, which is emitted based on an effective sky temperature, governs at night. On cold clear nights, this emitted radiation can reach low values and water on the earth's surface can freeze even though the ambient air temperature is above 0°C (Incropera and DeWitt 2002).

2.7 TEMPERATURE RELATED WORK ON BRIDGES IN THE UNITED STATES

Some work has been done on predicting temperature distributions in bridges to determine the corresponding thermal deflections and stresses. The American Association of State Highway and Transportation Officials (AASHTO) specifies a range of temperatures for moderate and cold climates that can be used to predict longitudinal thermal deformations for a bridge (Moorty and Roeder 1992). To develop a better way to account for the complexity of thermal deflections, including those in directions other than the longitudinal, field tests have been compared to simulation models. Moorty and Roeder used available weather data in combination with a finite element model (ANSYS). Results from this work showed that the mid-to-late afternoon during the summer months and the early morning of the winter months tended to be periods when thermal deformations were the most critical. In addition to the heat transfer principles used to simulate thermal distributions in other research, the work by Hunt and Cooke (1975) included the low frequency radiation loss from concrete bridges at night due to low values of atmospheric radiation. This loss accounted for bridge temperatures being colder than the ambient air temperature at night and was included in a simulation model by applying a negative radiation.

CHAPTER 3

Material Properties

3.1 WEATHERING STEEL

In order to predict the thermal response of a weathered steel guideway at any location in the country, a correlation must be established between the meteorological data available in a particular region and the temperature of guideway members. Preliminary experiments were performed to first determine a general connection between how the temperature change of small steel plates related to the change in solar radiation over the same time period. Since weathering steel is being considered for use with the Maglev train guideways, these same tests were used to compare the response of weathered plates to that of black and bright silver plates, under the same conditions.

In order to develop an accurate finite element model to determine the stresses and deformations caused by a temperature gradient over the guideway for the Maglev train, information on the material properties of weathering steel and how temperature varies transversely and longitudinally throughout a girder must be collected. Additional experiments were therefore performed to determine the material properties needed to accurately predict the change in temperature over time for a particular material. Properties including the reflectivity, emissivity, and convection coefficient of a typical weathering steel plate were therefore determined. This chapter will describe these experiments and what information the results provide on how heat is transferred to and from weathering steel.

3.2 INSTRUMENTATION

A majority of the data described in this report was collected using a datalogger. Using user-defined inputs for each measuring device, the datalogger converted recorded voltages from various sensors into temperature and radiation values. Additional measurements were taken from two weather stations operated by the Concrete Durability Center (CDC) near the project site. Weather data was also taken from two U.S. National Weather Service weather stations in the Austin, Texas area, KAUS and KATT. The tests described in this chapter were conducted on various days between the months of July and November 2004. A description of the weather conditions on days that tests were performed is found in the Appendix of this report.

3.2.1 Thermocouples

Thermocouples are devices that produce a voltage that is proportional to a temperature. They consist of two dissimilar metals that are joined at one end to form what is called a measuring junction. This measuring junction was placed at the location where the temperature was desired. For this project, the other ends of both of the metals were connected to a datalogger where they formed what is called a reference junction. Typically reference junctions are kept at a specified temperature, such as the ice point for water. However, the datalogger used the temperature of its panel as the reference junction temperature. The temperature difference between the reference junction and the measuring junction related to a voltage that the thermocouple output to the datalogger. If the junctions were at the same temperature, the output voltage would be zero (Figliola and Beasley 1995).

Type J thermocouples constructed of 24 gauge iron and constantan wires were used exclusively on this project. The measuring junction was formed by spot welding the iron and constantan wires together.

3.2.2 Pyranometers

Pyranometers are used to measure solar radiation by producing a voltage that can be converted by a datalogger. How pyranometers produce this voltage depends on the type of sensor it uses. Two different radiation sensors were used during this project. The radiation data for the initial experiments of this project was gathered by a Li-Cor LI200X silicon pyranometer used by one of the CDC affiliated weather stations. The LI200X used a photovoltaic detector, had a response time of 10 μ s, and had a light spectrum waveband of 400 to 1100 nm (CSI 1997). Radiation data from this weather station was used until the station was moved during the first week of August 2004.

To replace this source of data, a CM3 pyranometer manufactured by Kipp & Zonen BV was used. This pyranometer converted the solar radiation into heat and used a thermopile sensor to translate the resulting temperature difference into a voltage (CSI 2002). The CM3 was attached to the datalogger on September 7 2004 and was used throughout the remainder of the project. The CM3 had a 95% response time of 18 seconds and a 50% points spectral range of 305 to 2800 nm. The CM3 therefore had a slower response time than the LI200X, but could be used over a larger spectrum of wavelengths. The spectral range of the CM3 allowed it to be inverted to measure reflected solar radiation. Figure 3.1 shows photographs of the two pyranometers used on this project.

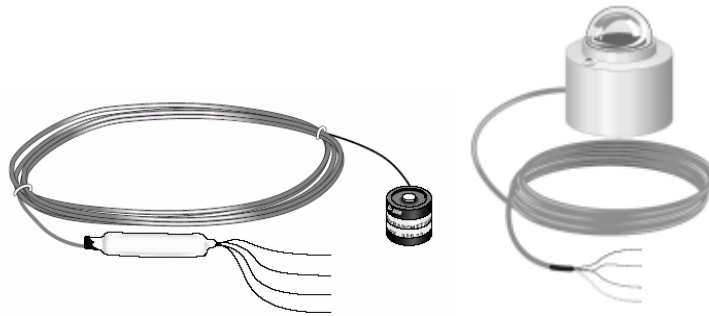


Figure 3.1 Pyranometers: LI200X and CM3 (CSI 1997 and CSI 2002)

3.2.3 Datalogger

The 21X Micrologger manufactured by Campbell Scientific, Inc. (CSI) was the datalogger used to gather data by connecting thermocouples and a pyranometer to its differential voltage channels. The datalogger performed user-defined calculations using input information and output the corresponding temperature and radiation values. For this experiment, weather data was transferred to a computer through a serial port and a converter cable. Figure 3.2 shows a photograph of the type of datalogger used throughout this project. For multiple day experiments, the 21X was generally programmed to collect data every ten minutes. Shorter intervals were used for tests with durations shorter than one day.



Figure 3.2 Photograph of 21X Micrologger

3.2.4 Additional Weather Stations

The second CDC weather station remained near the project site throughout the duration of the project. Data used from this station included wind speed and ambient air temperature. The two National Weather Service weather stations referred to in this report recorded conditions at Camp Mabry (KATT) and Austin Bergstrom International Airport (KAUS). KATT and KAUS were approximately 5 and 13 miles from the project site, respectively. Data taken from the CDC and National Weather Service stations will be designated as such. All other data was measured using the instrumentation operated by the writer of this report.

3.3 PREPARATION OF STEEL PLATES WITH DIFFERENT SURFACE CONDITIONS

To determine how the thermal response of weathering steel compares to other surfaces, small steel plates with three different surface conditions were analyzed. Steel plates with surfaces that were weathered, painted ultra flat black, and painted bright silver were therefore exposed to solar radiation while their temperatures were monitored over time.

A total of six ten-inch by ten-inch plates, summarized in Table 3.1, were cut from a $\frac{5}{8}$ -in. thick plate that had weathered from sitting outdoors after use in a previous project. The two most evenly weathered plates were placed outside on a sheet of plastic and periodically covered with water in order to rust the plates more evenly before beginning the experiment. The four remaining plates were sandblasted to remove the existing rust and mill-scale to ensure that the silver and black spray paint would adhere to the surface. One of the weathered plates was also sandblasted on all of its surfaces except the top face. This was done to determine the effects of having different surface conditions on either side of the steel weathered and silver painted plates, to mimic closed girders.

Table 3.1 Summary of Steel Plates

PLATE	COLOR (TOP)	COLOR (BACK & SIDES)
1	Weathered	Weathered
2	Weathered	Ultra Flat Black
3	Bright Silver	Bright Silver
4	Bright Silver	Ultra Flat Black
5	Ultra Flat Black	Ultra Flat Black
6	Ultra Flat Black	Ultra Flat Black

After sandblasting the appropriate plate surfaces, a $\frac{3}{8}$ -in. diameter hole was drilled $\frac{3}{8}$ in. deep into the center of the underside of all six plates. After the plates were spray painted, a thermocouple was inserted into the hole and attached to the plate using epoxy to measure the plate temperature near mid-depth. A cross section of the plates is shown in Figure 3.3.

A stand for the plates, constructed of wood 2x4s in a grid pattern, was used to prevent the plates from resting directly on the ground and to allow some airflow to reach the underside of the plates. The plates were positioned horizontally to prevent direct solar radiation from hitting their underside. Since the plate stand was open to allow airflow, the plates were also exposed to indirect solar radiation reflected from the objects below the stand.

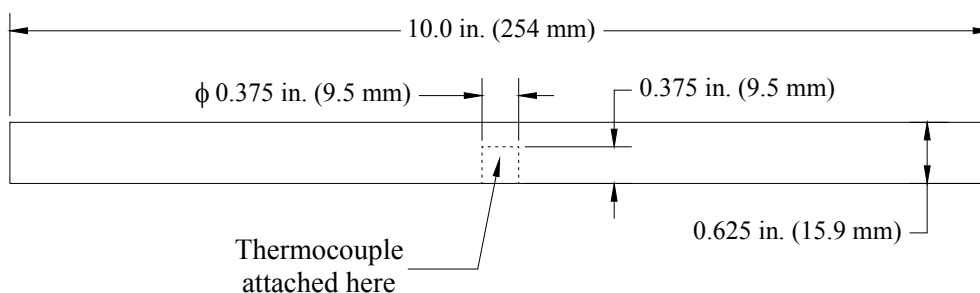


Figure 3.3 Cross Section of Test Plates

3.4 CALIBRATION

The thermocouples were calibrated to check their accuracy. Thermocouples attached to the small steel plates were tested in an air-conditioned room and in a freezer to test their response at two temperatures and to check that they were not damaged during their connection to the plates. Thermocouples not attached to the plates were typically constructed on an as needed basis. Since these thermocouples were typically checked individually and only at one temperature in an air-conditioned room, a mid-project calibration was performed. This process involved calibrating all existing and newly constructed thermocouples not already attached to a steel plate in an ice bath and in boiling water. The measured temperatures for each thermocouple were compared to the expected values for the freezing and boiling points of water, 0°C and 99.3°C, respectively. These phase change temperatures were based on the altitude of the calibration location measured by a Global Positioning System to be 700.3 ft above sea level. For this altitude, the external pressure was measured to be 740.9 mm*Hg (NOAA 2005), which when substituted into a curve fit of known data points of saturated vapor pressure of water versus temperature, resulted in the boiling point of 99.3°C (Giancoli 2000). Averaging the deviation of each thermocouple yielded errors ranging from 0.10 to 0.57°C for the freezing point and -0.01 to -0.75°C for the boiling point. These errors were determined to be accurate enough for the scope of this project.

3.5 EFFECT OF SURFACE CONDITIONS

For an initial outdoor experiment, the plate stand was placed at a site maintained by the Concrete Durability Center (CDC). This site was chosen because it was a large unshaded area and the two active weather stations operated by the CDC were nearby. During the initial three-day outdoor period, the stand

was placed at ground level on a gravel surface. Figure 3.4 shows that the bottom surfaces of the plates sat 3.5 in., the long edge of a wood 2x4, above the surface on which the plate stand was placed. The datalogger was housed in an all-weather box that was wrapped with a plastic sheet to provide additional protection from possible rain. The objective of this test was to compare the measured temperatures of the plates to the solar radiation and the ambient air temperature measured by both nearby weather stations and a thermocouple connected to the datalogger. An additional objective of this test was to begin determining the effect of the different surface conditions on the plate temperature.



Figure 3.4 Photograph of Plate Stand

A plot of the data from the initial three-day test near the weather station is shown in Figure 3.5. This figure shows that the temperature of the weathered plate follows the path of the solar radiation and the ambient air temperature. It is interesting to note that the correlation between the solar radiation and the temperature of the plate is also evident during a rapid drop in radiation on July 11 at about 4 PM. This drop was assumed to be due to cloud cover in the afternoon. It should also be noted that the radiation equals zero from the late evening until the early morning as expected.

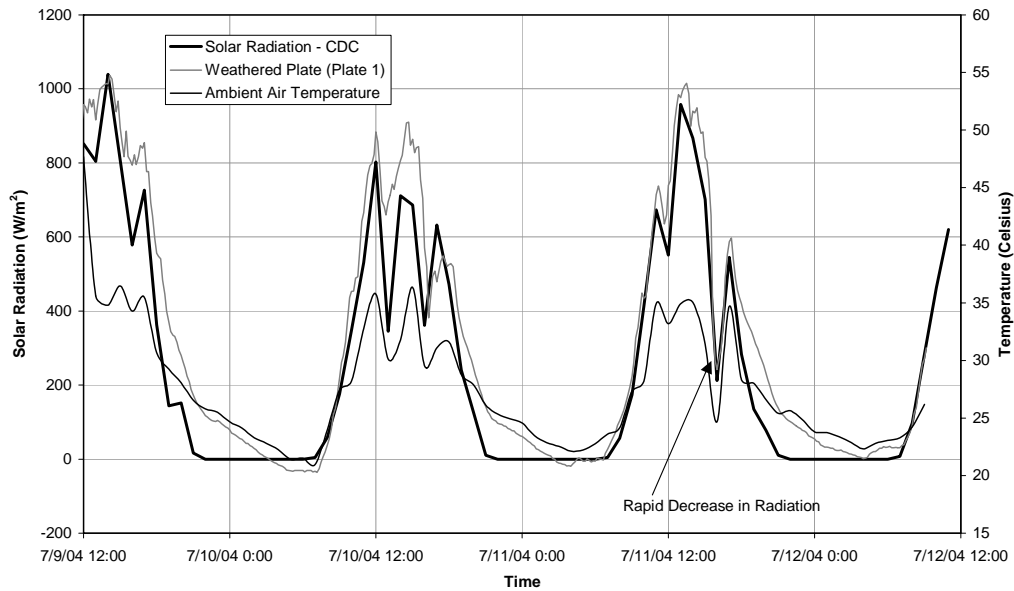


Figure 3.5 Solar Radiation & Temperature vs. Time (July 9-12 2004)

Figure 3.6 shows the effect of different surface conditions on the temperature of the small steel plates. The plate painted ultra flat black was intended to act as an approximate blackbody and as expected, it reached a higher temperature during the day than the other plates. The bright silver plate was intended to act as a highly reflective surface in comparison to the blackbody, and as expected, reached much lower maximum temperatures than the ultra flat black plate throughout the three-day sample. At night, the temperature of the black plate dropped below that of the other plates, while all of the plates reached temperatures lower than the ambient air temperature. This correlates to research findings on the temperature of concrete bridges at night (Hunt and Cooke 1975).

Figure 3.6 also shows that the weathered plate more closely followed the black plate than the silver plate. The results of the initial tests performed at ground level therefore suggest that the weathering steel will absorb significantly more energy and ultimately reach higher temperatures than a brightly painted surface and will behave similarly to an approximate blackbody.

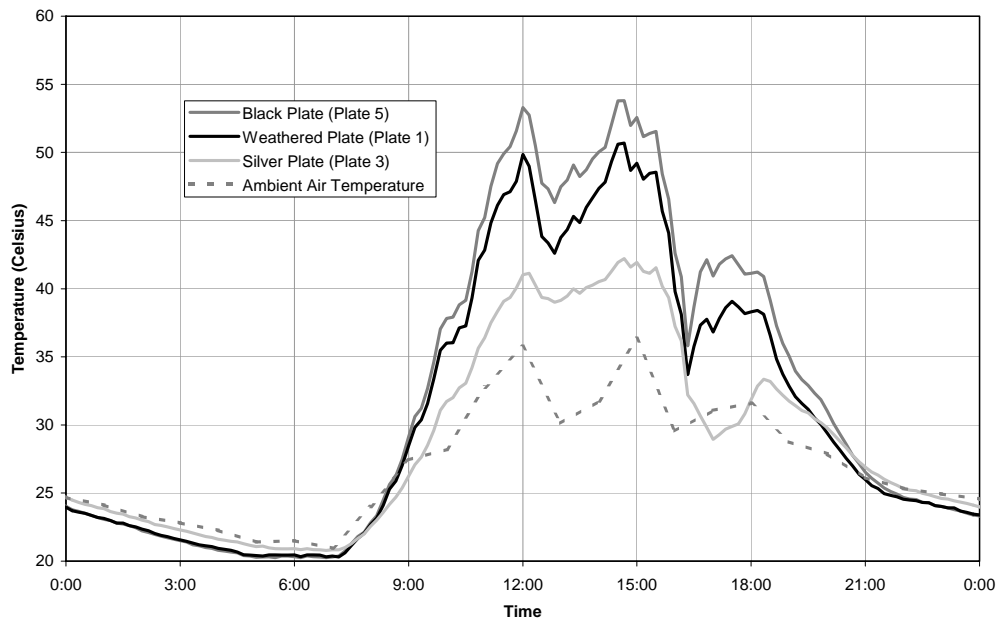


Figure 3.6 Temp vs. Time for Different Surface Conditions (July 10 2004)

3.6 EFFECT OF STEEL AREA AND GEOMETRY

In order to gather more information about the effects of different top and bottom surface coatings, the plates were placed on top of a full size weathered tub girder, as shown in Figure 3.7. The girder was used during a previous experiment at FSEL and was stored outside the building during the project. Thermocouples were placed near the test plates on the top and bottom flanges of the girder in order to compare the results of the small weathered test plates to the larger girder flanges. The temperature measurements from the flanges also served as preliminary tests on the temperature gradient experienced by a weathered steel girder. In order to obtain a better understanding of the solar radiation on the plates, a CM3 pyranometer was wired to the datalogger and attached to the west top flange of the girder near the plate stand.

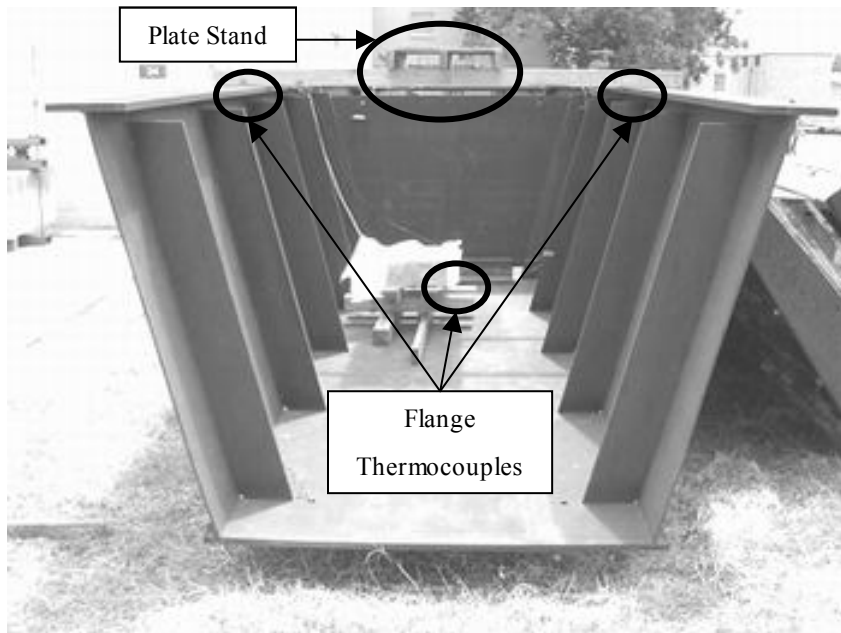


Figure 3.7 Test Setup for Plate Temperature Measurements

Figure 3.8 shows that as it did during the initial outdoor test, the weathered plate temperature follows the solar radiation data. The ambient air temperature measured by the datalogger also follows the general path of the solar radiation data, but reaches significantly higher temperatures than the maximum temperature of 35°C recorded by the CDC weather station. This large difference could be due to the datalogger ambient thermocouple being exposed to the sunlight during the sample instead of being positioned in the shade.

A comparison of the two weathered plates with different bottom coatings is shown in Figure 3.9. At some points during the day, the weathered plate with the black underside has a higher temperature than the fully weathered plate. However, the difference is small. The temperature difference between the plates is plotted as a dashed line using the axis on the right. The maximum difference was about 1°C.

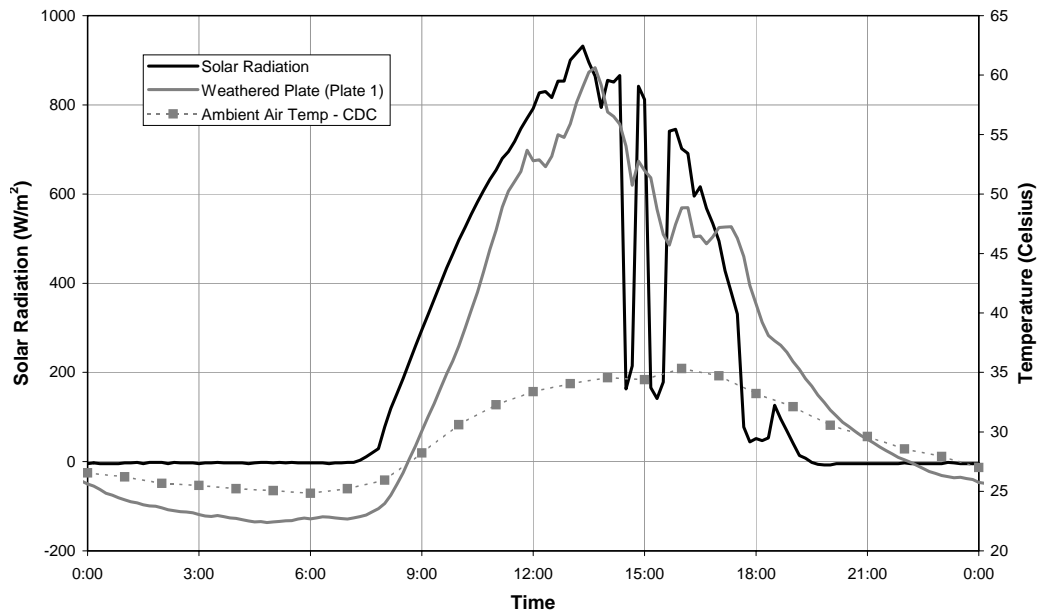


Figure 3.8 Solar Radiation & Temperature vs. Time (September 17 2004)

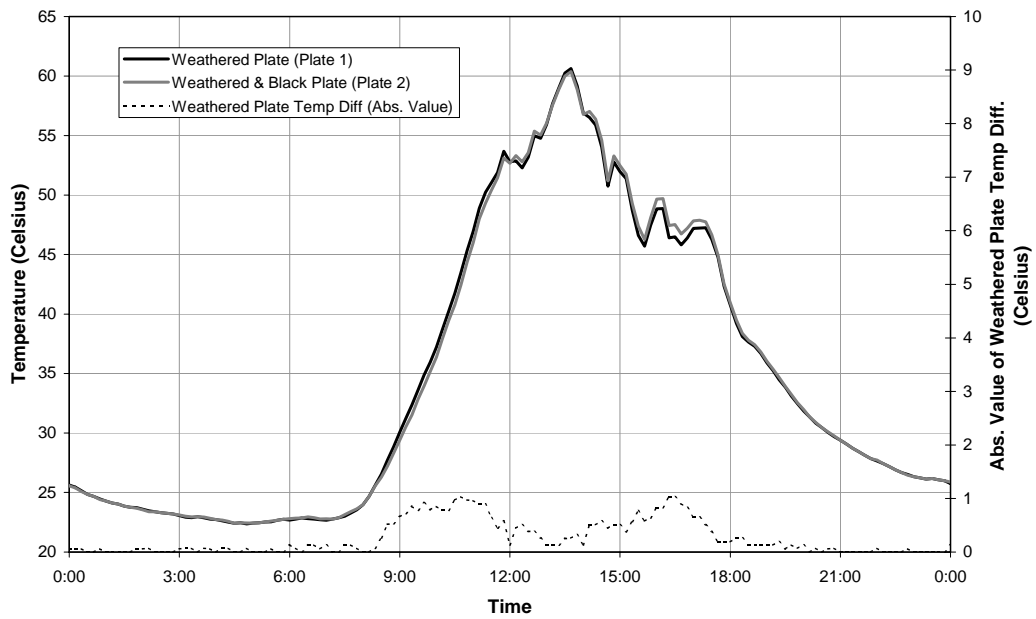


Figure 3.9 Bottom Coating - Temperature vs. Time (September 17 2004)

Figure 3.10 shows that while the top flange of the full size weathered girder follows the behavior of the weathered plate, the difference between the

flanges and the isolated plate is significant during the middle part of the day. Designing a full size girder for the extreme temperatures experienced by the smaller plates would be conservative. Figure 3.10 also shows that the temperature of the bottom flange does not closely follow that of the top flange or the weathered plate. This is due to the partial shading experienced by the inside of the open girder. At midday on September 17, the difference between the top and bottom flanges exceeds 16°C. For comparison, at a site in Germany, Transrapid International specified that the maximum positive difference in temperature between the top and bottom flange should be taken as 25°C (TRI 2000). Further experiments were performed on the temperature distribution over the cross section of the girder and will be discussed in the following chapter.

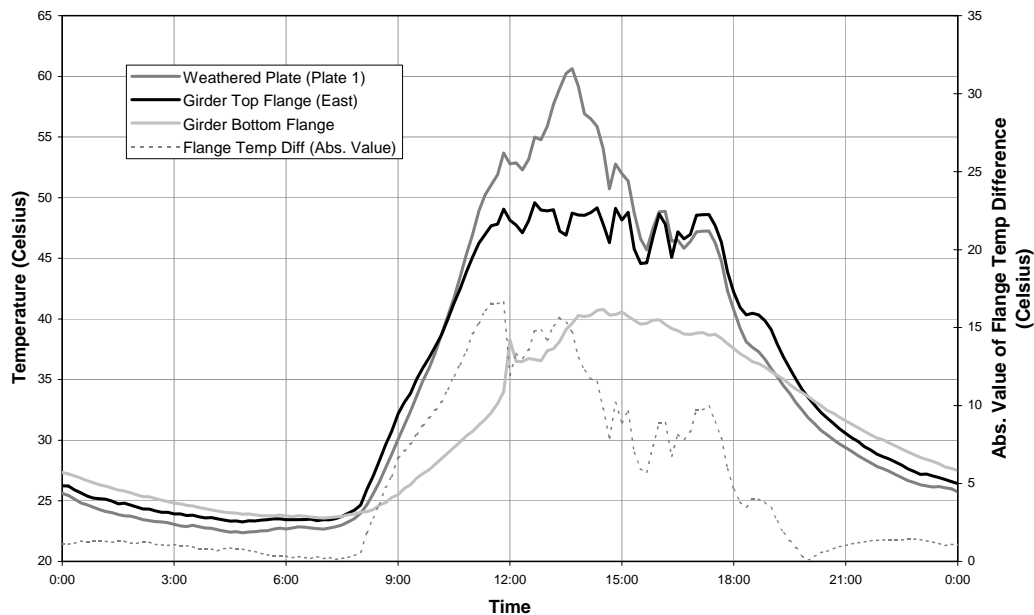


Figure 3.10 Plates & Girder – Solar Radiation & Temp vs. Time (Sept 17 2004)

3.7 SOLAR REFLECTIVITY

Reflectivity is defined as the percentage of the incoming radiation that is reflected by a surface (Incropera & DeWitt 2002). Surfaces with low reflectivity

values absorb more radiation and reach higher temperatures than surfaces with high reflectivity values. An experiment was performed on the three solid color plates to determine the solar reflectivity of the ultra flat black, bright silver, and weathered steel coatings. A photograph of the pyranometer and the experiment setup is shown in Figure 3.11.



Figure 3.11 Solar Reflectivity Experiment Setup

The CM3 pyranometer used for this experiment rested on a plate that was attached to a frame of steel rods and a C-clamp. To minimize the “noise” from adjacent surfaces that would be detected by the pyranometer while it pointed down towards the top surface of the plates, the clamp was attached to a central point of a large weathered steel plate. The accuracy of the radiation measurements was related to both the position of the sensor in the horizontal x-y plane of the large steel plate and the vertical distance from the top plate surface to the base of the dome of the pyranometer. Placing the pyranometer too close to the

plates may have produced inaccurate results due to shadowing and local variation in plate surface texture and color.

The procedure for the reflectivity test involved measuring the solar radiation by pointing the pyranometer towards the sun and measuring the radiation reflected off the plate by pointing the pyranometer down towards the plate surface. Radiation readings were taken with the plates in seven different positions, spaced 2.5 in. apart. The plates were moved to these seven positions with the pyranometer centered on the width of the plate, as shown in Figure 3.12. This method made it easy to maintain a constant vertical distance between the radiation sensor and the plate, and maintained a constant lateral distance from the sensor to the edge of the large plate. A measurement cycle for this experiment was defined as first pointing the pyranometer up for one minute and then rotating it to point down for two minutes. Beginning with the second cycle, the small plates were shifted 2.5 in. to the next position while the radiation sensor was pointing upwards. Radiation readings were output to the micrologger every 20 seconds to allow enough time for the 18-second response time of the pyranometer and the time required to rotate the setup.

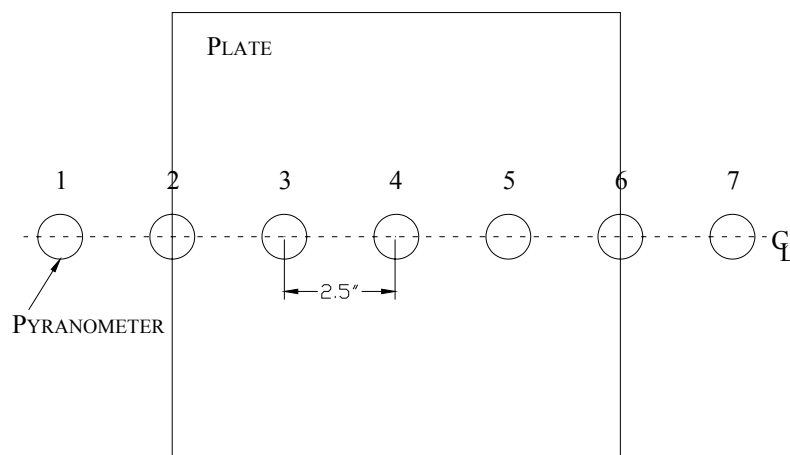


Figure 3.12 Movement of Plates underneath Pyranometer - Plan View

During the experiment, the plate being tested was placed on thin wood spacers to prevent the thermocouple attached to the bottom of the plates from being pressed between the large and small plates in addition to preventing effects due to conduction between the plates. Before reflectivity data was collected for the smaller plate, measuring cycles were performed over the large steel plate to determine its reflectivity. The reflectivity of the large plate was also tested after the cycles with the three small plates. The large plate was not moved underneath the pyranometer for these measurements. A significant difference between the results of these two tests on the large plate would indicate that the time of day and thus the angle of the sun might have affected the data for this experiment. For a similar check, the small weathered plate was also tested twice. Table 3.2 shows the experiment order and the time of day each plate was tested during the experiment.

Table 3.2 Order for Reflectivity Experiment (October 14 2004)

PLATE	START TIME	END TIME
Large Weathered Plate	3:43 PM	3:59 PM
Weathered Plate (Plate 1)	4:00 PM	4:30 PM
Black Plate (Plate 5)	4:32 PM	4:55 PM
Silver Plate (Plate 3)	4:59 PM	5:22 PM
Weathered Plate (2 nd Time)	5:26 PM	5:49 PM
Large Weathered Plate (2 nd Time)	5:50 PM	6:02 PM

The results of the reflectivity experiment are shown in Figure 3.13, which is separated into seven sections, each corresponding to one of the positions of the pyranometer relative to the small plates. Position 1 corresponds to when the centerline of the pyranometer was 2.5 in. from the edge of one of the small plates. When the pyranometer was directly above the edge of the plate, its location corresponded to Position 2. Since each position was spaced 2.5 in. from the

previous one, the plates were eventually moved to 2.5 in. beyond the far the edge of the small plate, or Position 7.

For this experiment, the solar reflectivity values were calculated by dividing each reflected radiation data point by the average of the solar radiation measurements from the same cycle. The first data point for both the upward and downward rotations was discarded to account for the pyranometer not being level and in place for the entire 18-second response time before the first measurement was taken.

The results of this experiment indicated that as expected, the black plate produced the lowest solar reflectivity. Similarly, the silver plate was expected to reflect a larger percentage of the incoming radiation and to therefore have the largest reflectivity values. In addition to confirming these expectations, Figure 3.13 shows how the solar reflectivity varies as the plates were moved underneath the pyranometer. The maximum reflectivity for the silver plate of 0.47 was calculated during Position 4, when the pyranometer was directly above the center of the 10-in. by 10-in. plate. This makes sense because this position corresponds to when the greatest surface area of the silver plate was directly beneath the radiation sensor and could therefore have the most dramatic effect on the output. The black plate also had its greatest effect on the pyranometer output and thus experienced its minimum reflectivity, 0.04, at Position 4.

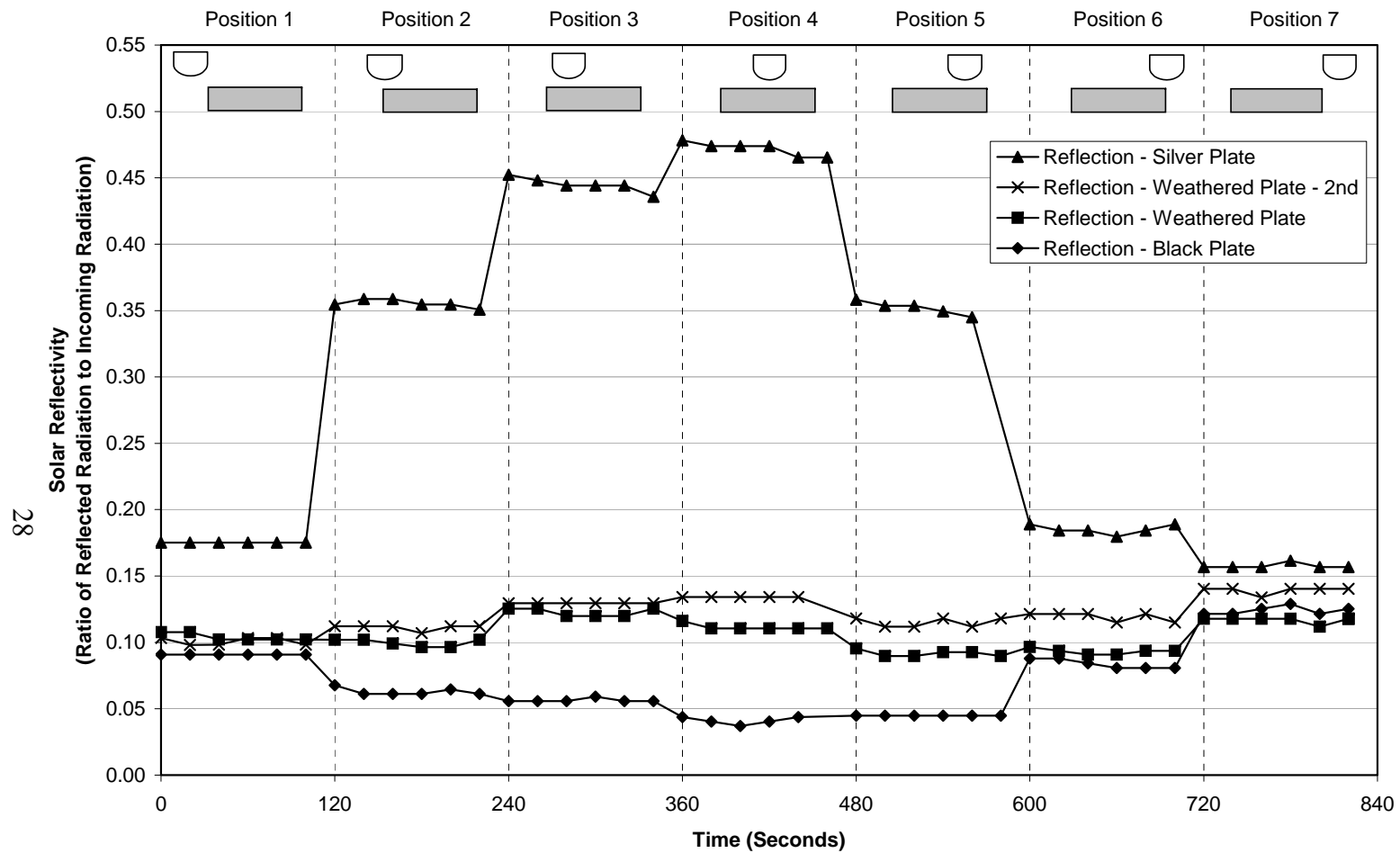


Figure 3.13 Solar Reflectivity vs. Time (October 14 2004)

The reflectivity value for the weathered plate of 0.12 was determined by averaging the values obtained from its two runs underneath the pyranometer. This reflectivity value is significantly closer to the value for the black plate than the value for the silver plate. The weathered plate will therefore absorb nearly as much energy and reach almost as high of a temperature as the black plate under direct sunlight. It should be noted that while one might expect Figure 3.13 to be somewhat symmetrical, with the reflectivity data for Position 3 matching the data from Position 5, this is not the case. Instead, as Figure 3.14 shows, the position of the sun during the afternoon caused readings for positions 3 and 5, and 2 and 6 not to be identical. For positions 5 through 7, the angle of the sun causes the pyranometer to record a larger percentage from the large weathered plate beneath the small plates than for positions 1 through 3. Radiation reflected off the large plate therefore has more of an effect on the later positions. This effect is the most extreme for the silver plate because the difference between its reflectivity and that of a weathered surface is significant.

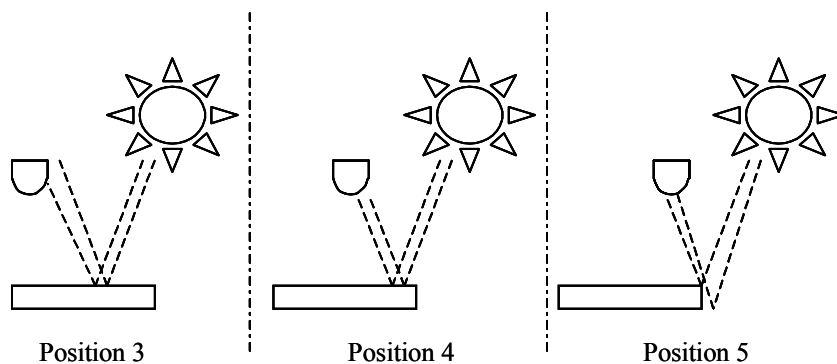


Figure 3.14 Plate Positions for Reflectivity Experiment

3.8 EMISSIVITY

The emissivity of a surface is the ratio of the radiation that the surface emits to the radiation a blackbody would emit at the same temperature. The

emissivity, ϵ , of a theoretical blackbody would be 1.0, but real surfaces can have an emissivity of about 0.95 (Hagen 1999). If a body is held within a large isothermal enclosure and Kirchoff's law is assumed, the absorptivity, or $1 - \text{reflectivity}$, equals the body's emissivity in all directions over all wavelengths (Incropera & DeWitt 2002). Although these conditions do not exist here, one minus the reflectivity will be used as an approximation of the plates used in this project. The approximate emissivities are therefore 0.96, 0.88, and 0.53 for the black, weathered, and silver plates, respectively. A thermodynamic text suggested that a rough oxidized steel surface had an emissivity of 0.92, which is close to the estimate of 0.88 (Ražnjević 1995).

Additionally, an approximation of the emissivity of the weathered plate was determined using an infrared sensor. For this test, the plate was held in an air-conditioned room while the datalogger recorded temperatures. Adjusting the emissivity input for the infrared sensor produced a range of temperatures for the surface of the weathered plate. Relatively accurate results were achieved within the range of 0.88 to 0.92 for the emissivity. An emissivity of 0.90 was assumed for the weathered plate throughout this project.

3.9 CONVECTION COEFFICIENT

Convection refers to the energy transfer caused by a fluid moving past a surface. The convection coefficient depends on the type of fluid, flow conditions, flow rate, and surface geometry. Experiments were performed using the small steel plates with weathered, bright silver, and ultra flat black surfaces to estimate this coefficient. However, since flow conditions and flow rate components are highly variable, future tests would be needed to determine the importance of accurately calculating the convection coefficient. The plates were first heated in an oven and then hung vertically in a non-temperature controlled room as they

cooled. Holes with a diameter of $\frac{5}{16}$ -in. were drilled through the plates so that $\frac{1}{4}$ -in. diameter hooks could be used to hang them. In addition to the temperature of the plates, the ambient air temperature was recorded during this experiment. Figure 3.15 shows the plates hanging vertically as they cooled.



Figure 3.15 Photograph of Test Plates Hanging After Being Heated in an Oven

After the plates were removed from the oven, a door near the experiment setup was opened for ventilation and the resulting breeze was capable of moving the piece of paper hung on the cross bar shown in Figure 3.15. The door was closed later in the cooling process. When analyzing the data, it was assumed that forced convection occurred while the door was open and that natural convection occurred while the door was closed. Separate calculations were performed to

determine the convection coefficient for the two conditions. The formula used for both conditions, Equation 3.1, included a radiation term and a convection term.

$$\frac{dT}{dt} = \frac{-1}{m \cdot c} \cdot \left[\varepsilon \cdot \sigma \cdot A \cdot (T_{o_i}^4 - T_{\infty_i}^4) + h \cdot A \cdot (T_{o_i} - T_{\infty_i}) \right] \quad (\text{Equation 3.1})$$

where

$$m = \text{mass} = 8.03 \text{ kg}$$

$$c = \text{specific heat for steel} = 480 \text{ J / (kg} \cdot \text{K)}$$

$$\varepsilon = \text{emissivity} = 0.90 \text{ [unitless]}$$

$$\sigma = \text{Stefan - Boltzmann's constant} = 5.67 \cdot 10^{-8} \text{ W / (m}^2 \cdot \text{K}^4)$$

$$A = \text{total surface area of plate} = 0.145 \text{ m}^2$$

$$T_{o_i} = \text{temperature of the plate at time } i \text{ [K]}$$

$$T_{\infty_i} = \text{temperature of the ambient air at time } i \text{ [K]}$$

$$h = \text{convection coefficient [W / (m}^2 \cdot \text{K)]}$$

The values for the Stefan-Boltzmann's constant and the specific heat of steel were taken from a heat transfer text (Incropera and DeWitt 2002). The mass, surface area, and emissivity values for the weathered plate were taken from the experimental results of this project. Plots of Equation 3.1 using these values and different values for h were compared to the recorded cooling curve of the weathered plate. Although the hooks used to hang the plates were also heated in the oven to minimize temperature loss due to conduction, any conduction loss from the hooks to the horizontal pole they hung on was not accounted for in these calculations.

The plates were heated until the warmest plate approached 175°C. The temperatures of the plates at the onset of the forced convection were measured to be 171.6°C, 155.3°C, and 146°C for the black, weathered, and silver plate, respectively. Figure 3.16 compares the initial cooling of each plate. For the weathered plate, a convection coefficient of 8.0 W/(m²*K) produced the lowest maximum absolute error when compared to the recorded results. Figure 3.17

shows the recorded cooling data versus the plot of the differential equation with $h = 8.0 \text{ W}/(\text{m}^2 \cdot \text{K})$ and the ambient air temperature at each time step. The largest absolute error calculated between the differential equation curve and the recorded data was 1.39°C . Values of 7.8 and $7.5 \text{ W}/(\text{m}^2 \cdot \text{K})$ were calculated using the same procedure for the black and silver plates, respectively. A third curve on the plot represents the expected cooling of the weathered plate for the same conditions and convection coefficient, but without the radiation component. The difference in temperatures between the two differential equation curves shows that both the radiation and the forced convection components significantly contribute to the heat transfer of the plate. However, the contribution of the convection component does appear to be larger. The ambient air temperature of the room during this period ranged from 14.0 to 16.8°C .

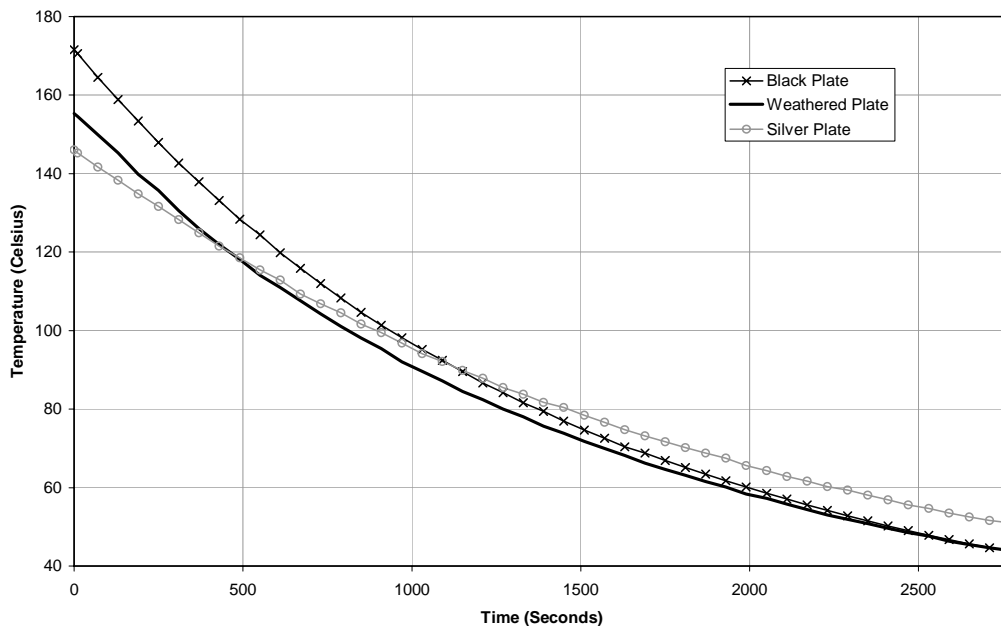


Figure 3.16 Comparison of Cooling Curves for Three Plates (Nov 12 2004)

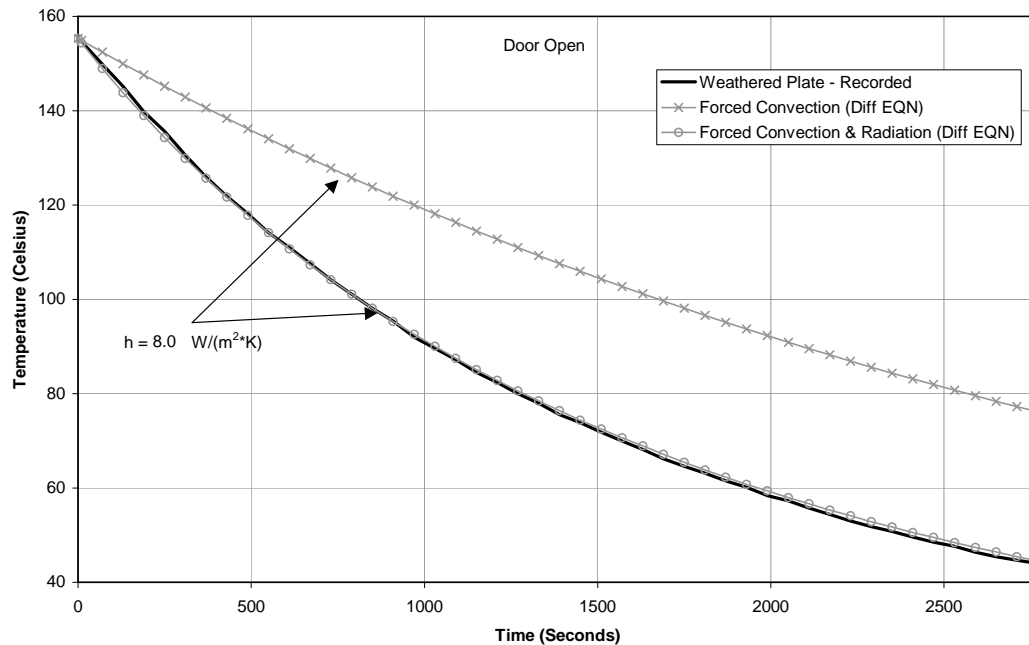


Figure 3.17 Temperature vs. Time – Forced Convection (November 12 2004)

The temperatures of the plates after the door were closed to eliminate wind current in the room were 43.8°C, 43.8°C, and 50.8°C for the black, weathered, and silver plates, respectively. Closing the door caused the ambient air temperature to level off at about 18°C. For the weathered plate, the lowest maximum absolute error for the period of natural convection of 0.46°C resulted from a convection coefficient of 4.6 W/(m²*K). Values of 4.6 and 4.4 W/(m²*K) were calculated using the same procedure for the black and silver plates, respectively. In addition to the curves representing the recorded cooling data for the weathered plate, the differential equation curves including and excluding radiation, are shown in Figure 3.18. Again the difference between the two differential equation curves demonstrates that convection contributes more to the heat transfer than the radiation component, but both contributions are significant.

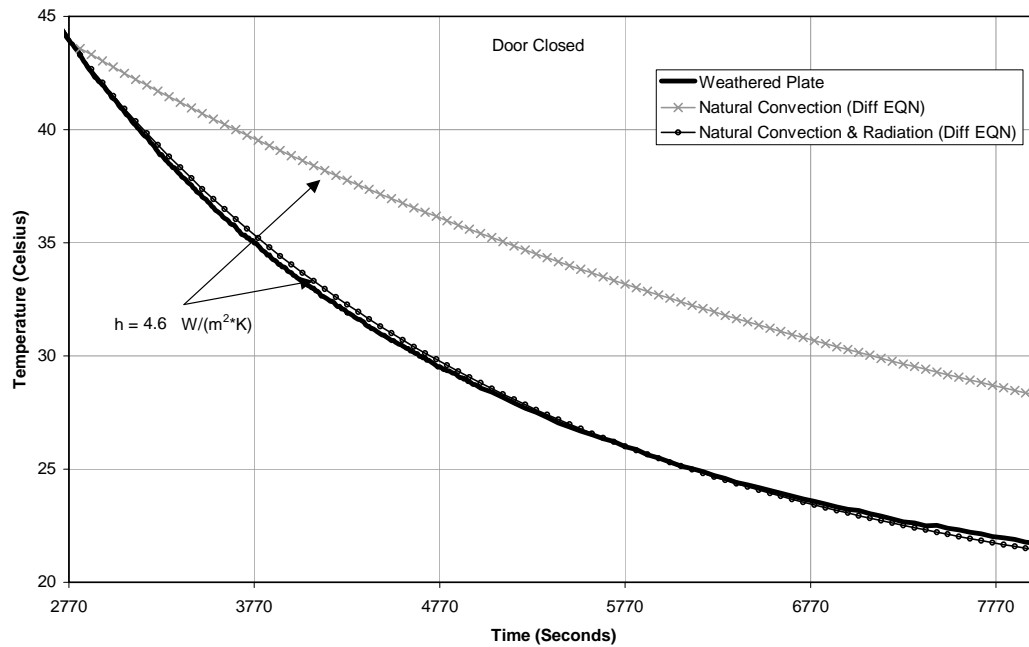


Figure 3.18 Temperature vs. Time – Natural Convection (November 12 2004)

3.10 CONCLUSIONS

Recording the thermal response of the small steel plates while they were exposed to solar radiation demonstrated that the weathered plate behaved similarly to the plate painted ultra flat black. It therefore appears that girders constructed of weathering steel will behave relatively close to a blackbody under thermal loading. Tests on a full size girder will provide a more detailed assessment of the temperature gradients a Maglev guideway constructed with weathering steel might develop. These tests will be described in Chapter 4.

Using the reflectivity, emissivity, and convection coefficients described in this chapter, an initial prediction can be made for the temperature of the weathered plate over time. A third term will be added to Equation 3.1 to account for the solar radiation absorbed by the plate. Also, the influence of the convection coefficient will be explored, as the results using a constant convection coefficient

will be compared to results using a convection coefficient that varies with the wind speed at a given time. These predictions are discussed in Chapter 5.

CHAPTER 4

Girder Properties

4.1 DESCRIPTION AND LOCATION OF GIRDER

Temperature measurements were gathered from a 54-ft. long full size weathered girder that sits outside Ferguson Laboratory. The girder was moved outside the laboratory after it was used in an earlier project. This experimental data was collected to provide measurements to compare with three-dimensional analytical predictions. These measurements included the distribution of temperature over a single cross section over several days during November and December 2004. They also included the temperatures at various cross sections on a single clear day. Thermocouples were used to measure the variation of a single cross section, while an infrared thermometer was used to measure the longitudinal variation. The cross-section and dimensions of the girder are shown in Figure 4.1.

To better simulate an elevated guideway and to allow wind to reach the bottom flange, the girder was lifted off the ground and placed on two large concrete blocks. As a result, the bottom flange of the girder was raised an average of forty inches off the ground and positioned an average of about seven feet away from the exterior wall of Ferguson Laboratory. Throughout the monitoring of the girder, weather data including wind speed and ambient air temperature was recorded by the weather station operated by the Concrete Durability Center (CDC). Figure 4.2 shows the location of the girder relative to Ferguson Laboratory and the CDC weather station.

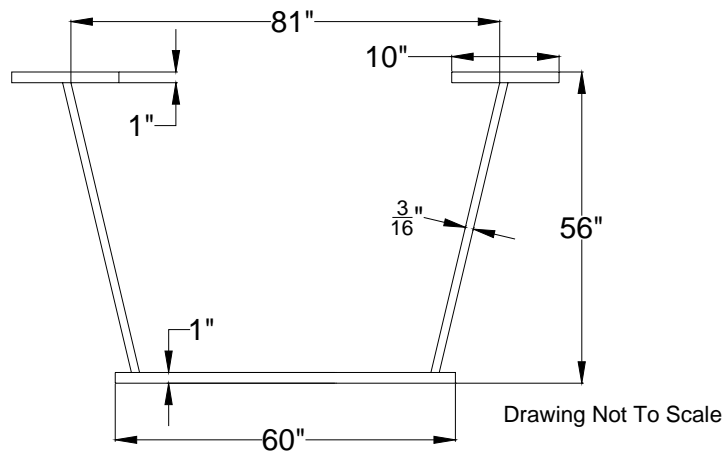


Figure 4.1 Cross Section of Full Size Girder

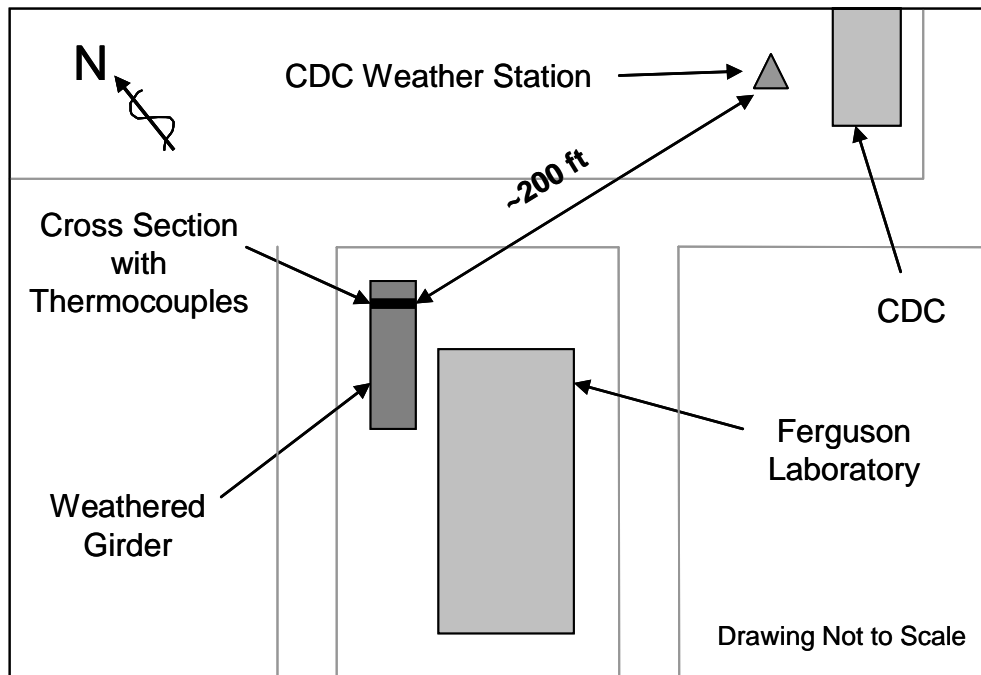


Figure 4.2 Map of Girder Location

4.2 EXPERIMENT SETUP

Thermocouples were used to monitor the surface temperature at seventeen locations over a cross section five feet from the northern end of the girder. Each top flange and web was monitored by three thermocouples while five were placed on the bottom flange. A CM3 pyranometer was attached to the west top flange near this cross section to monitor the solar radiation. A photograph of the test setup is shown in Figure 4.3.

Since the 21X Microloggers used on this project only provided eight input channels, an AM416 Multiplexer with thirty-two differential voltage channels was connected to the datalogger to increase the number of sensor inputs. Although all the thermocouples used during this experiment were attached to the multiplexer, the pyranometer was wired directly to the datalogger. Both the multiplexer and the datalogger were placed in an aluminum all-weather-box covered with plastic wrapping for additional protection.

In order to check the accuracy of the datalogger output for the thermocouples attached to the multiplexer, a calibration test was performed using ice and boiling water baths. As with the previous mid-project calibration, the freezing and boiling points of water were assumed to be 0°C and 99.3°C, respectively, at an elevation of about 700 ft. Deviations from the expected values were averaged for each thermocouple and resulted in errors ranging from 0.23 to 0.64°C for the freezing point and -0.80 to 0.30°C for the boiling point. These errors were determined to be accurate enough for the scope of this project.

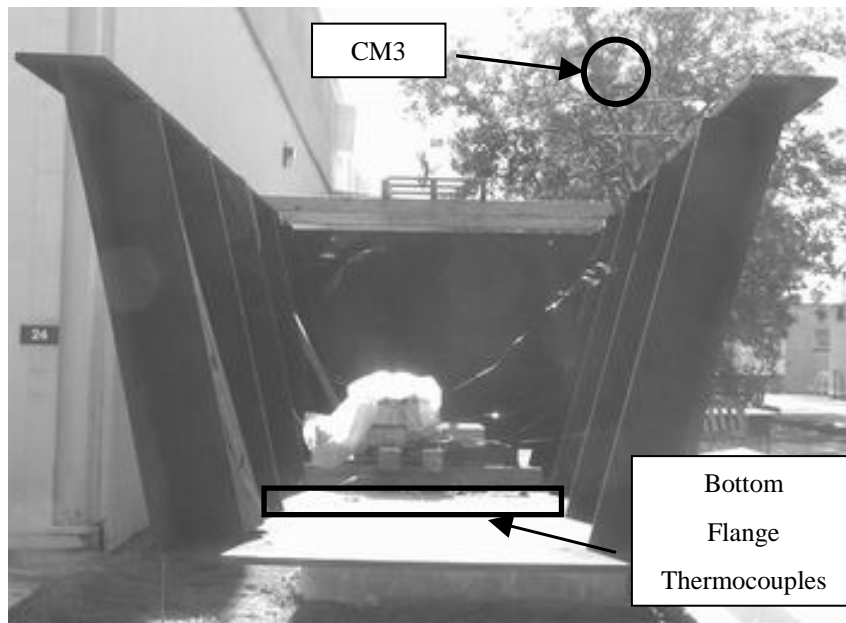


Figure 4.3 Test Setup for Thermal Gradient Measurements

Washers and self-tapping screws were used to attach each thermocouple and maintain its contact with the girder. Holes with slightly smaller diameters than the screws were drilled through the girder plates for ease of installation. To minimize the damage to the thermocouple, the self-tapping screws were tightened with a hand ratchet. A photograph of the thermocouple attachment is shown in Figure 4.4. Since the screw heads remained above the plate surface after tightening they may have experienced more convective cooling or heating than the adjacent surface of the girder. This could have altered the measured temperatures of the girder surface, but the effect was assumed to be small and was neglected in the analysis.



Figure 4.4 Attachment of Thermocouple to Girder Surface

4.3 VERTICAL TEMPERATURE GRADIENT

In order to calculate the temperature deflections of a weathered steel girder, the temperature gradients must be determined. This experiment was performed to measure the maximum values for the vertical and lateral gradients experienced by the girder as well as the weather conditions that caused these extreme values. The maximum vertical gradient was experienced on December 11. Figure 4.5 shows how the solar radiation, ambient air temperature, and the temperature of the west top flange varied throughout this day. The west top flange was chosen because the pyranometer was located there. Due to partial shading of the girder during the day, thermocouples on members further from the pyranometer would less accurately represent the effect of the solar radiation at a

given time. For comparison, December 12 was also included in Figure 4.5. Classification of the weather during this two-day sample, in addition to other days described in this chapter, is found in the Appendix.

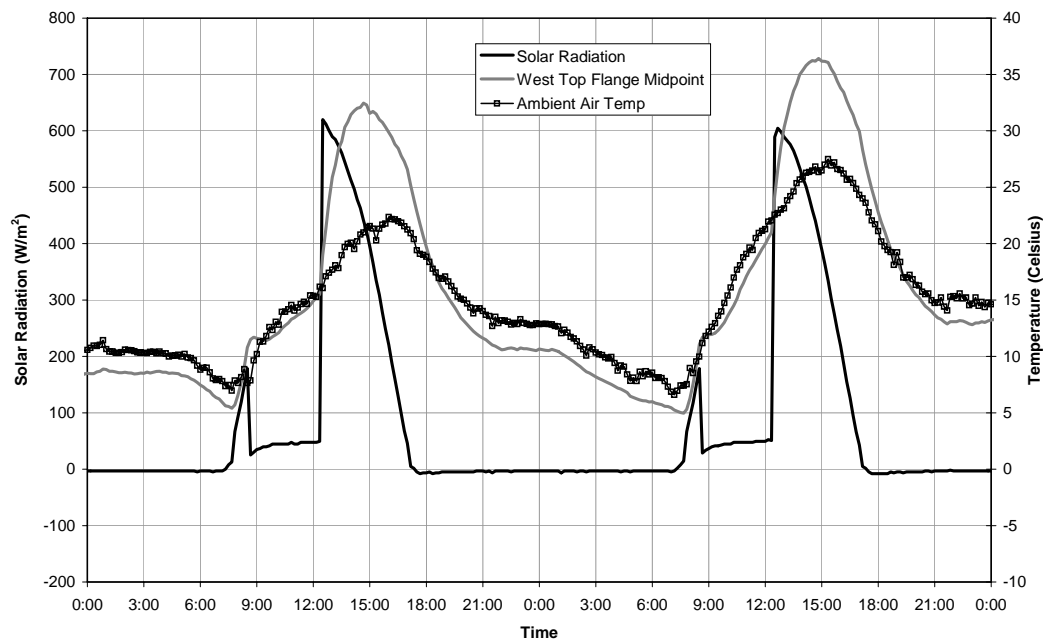


Figure 4.5 Solar Radiation & Temp vs. Time (December 11-12 2004)

During both days of the sample shown in Figure 4.5, the solar radiation reached two distinct peaks. The initial peak was caused by sunlight coming over the horizon in the early morning and hitting a portion of the girder that extends beyond the building. The initial decline associated with this peak occurred at about nine o'clock when the sun moved behind the laboratory building and the girder became shaded. The second radiation peak occurred when the sun came out from behind the building and the west top flange of the girder and thus the pyranometer, received direct sunlight. While the girder was in the shade, the west top flange temperature followed the path of the ambient air temperature. However, the girder quickly became warmer than the ambient air when it was exposed to direct sunlight.

Figure 4.6 shows a plot of the temperatures measured at the midpoints of the bottom and the two top girder flanges over the same two-day span. The vertical gradient was calculated by taking the largest difference in temperature of the six thermocouples on the top flanges from the five sensors on the bottom flange. The curve on the bottom of the plot represents the measured gradient.

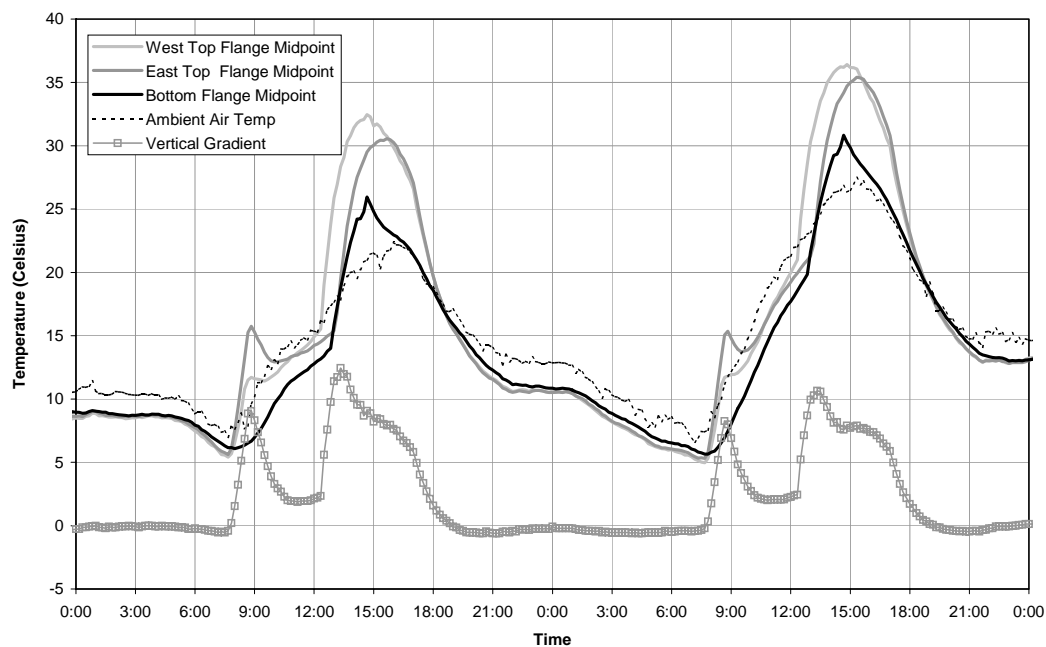


Figure 4.6 Flange Temperatures vs. Time (December 11-12 2004)

The maximum vertical gradient throughout this experiment was measured at 1:20 PM on December 11 to be 12.5°C. Figure 4.7 shows the distribution of temperatures in the girder at this time. The thick lines represent the shape of the girder and the hollow circles mark the relative locations of the thermocouples. The cross section is arranged with the eastern web on the left side of the page and the western web on the right side. The temperature measured by each thermocouple is shown at a perpendicular offset from the corresponding plate. Thermocouples near the intersection of two of the girder plates were included on the distribution of both members.

For reference, a dotted line representing a benchmark temperature runs parallel to each plate. In Figure 4.7, the benchmark of 20°C can be used to compare the thermocouple measurements at each location. For example, the data point associated with the midpoint of the western web is positioned to the left of the benchmark temperature line and therefore is at a temperature higher than the 20°C. The ambient air temperature is also shown as a reference at the midpoint of each girder plate.

A photograph of the girder taken at one o'clock a few days before the maximum vertical gradient was measured is included to help understand the cause of the temperature distribution. The sunlight visible on the right side of the girder and the shade on the left side correlate with the temperature measurements. The vertical gradient calculated at this time was due to the eastern part of the bottom flange being shaded by the building while the western top flange was experiencing direct sunlight. Although 12.5°C was the largest measured vertical temperature gradient during this experiment, it was not uncommon to measure a gradient over 10°C in the early afternoon on other clear days. The maximum lateral temperature gradient is discussed in Section 4.4.

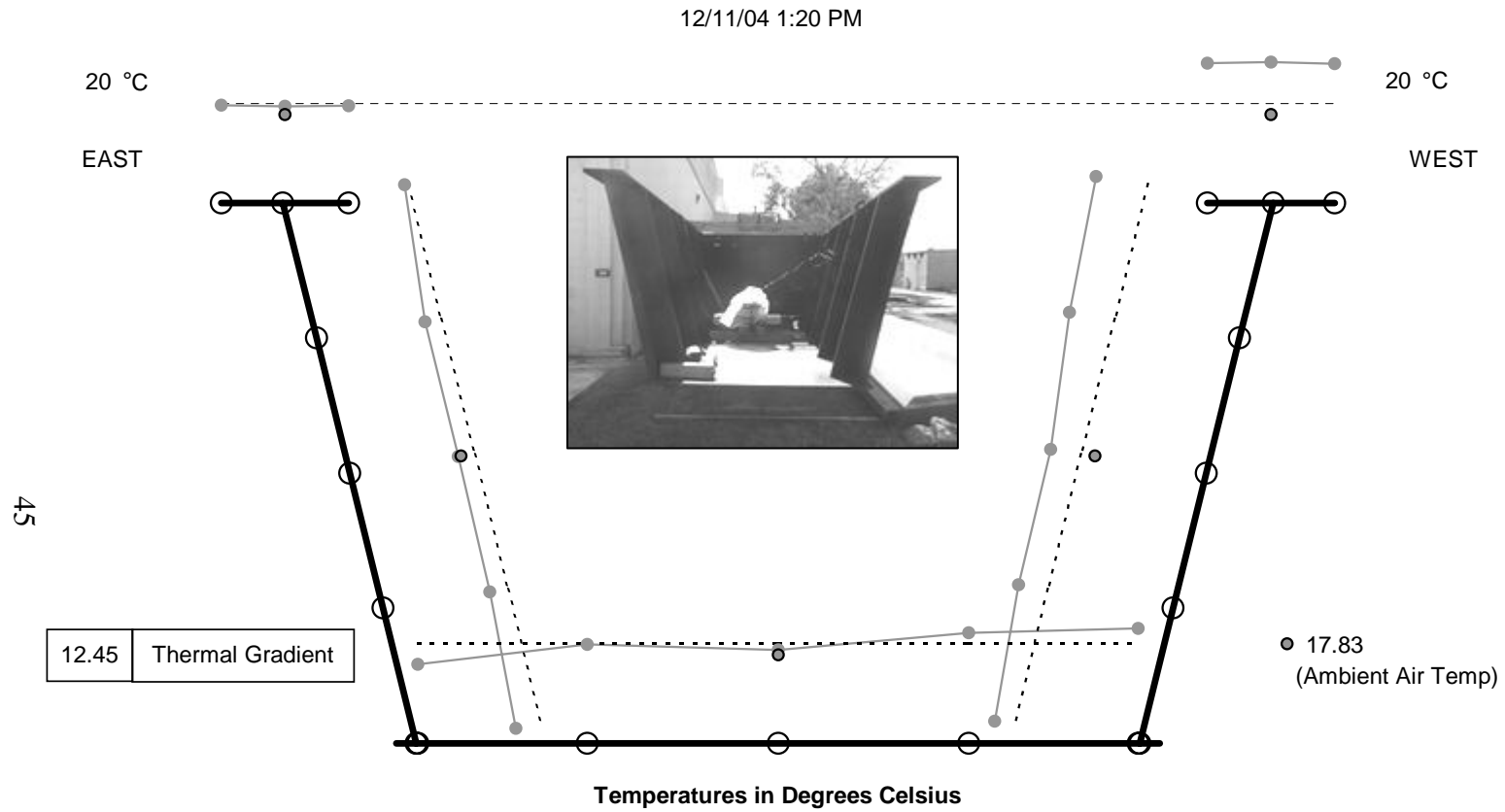


Figure 4.7 Girder Cross Section at Maximum Vertical Temperature Gradient

4.4 LATERAL TEMPERATURE GRADIENT

Temperature differences between the top and bottom flanges of the girder occurred due to shading of one plate more than another. Shading is also expected to affect the temperature difference between the eastern and western sides of the girder and thus the lateral gradient. The effect on the webs was expected to be more severe because during the early morning and late afternoon, when the sun is not directly above the girder, one side receives considerably more sunlight than the other. Wind moving in the direction perpendicular to the length of the girder is also expected to have an effect on differential cooling. The radiation data for the day on which the maximum lateral temperature gradient was measured, November 25, is shown in Figure 4.8.

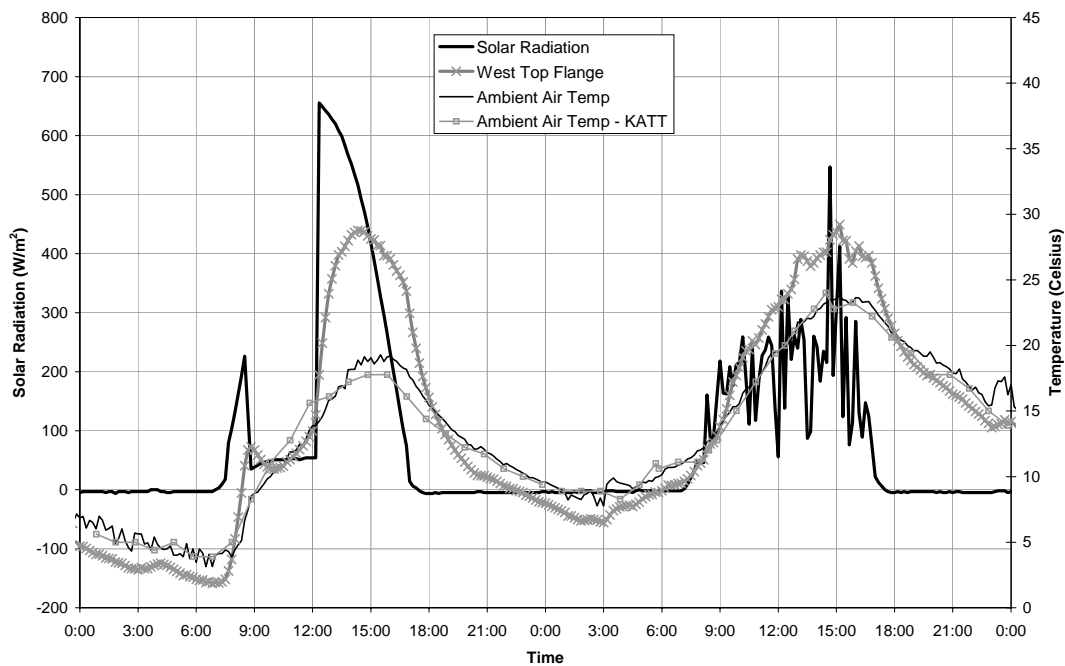


Figure 4.8 Solar Radiation & Temp vs. Time (November 25-26 2004)

As with the December 11-12 radiation plot, Figure 4.8 shows the temperature of the top west flange following the ambient air temperature when the

plate was not exposed to direct sunlight and quickly heating up in response to sunlight hitting the girder. The radiation data for November 26 fluctuated significantly while the data for November 25 was smooth similar to what was observed in Figure 4.5 for the December 11-12 sample. This fluctuation is due to the pyranometer being shaded by clouds on December 26. Table 4.1 lists the weather conditions observed during these periods at a National Weather Service station at Camp Mabry (KATT) about five miles from the project site. The smooth data for November 25 correlates to the clear conditions throughout the day, while the fluctuations on November 26 correspond to the mostly cloudy and overcast conditions.

Although the temperature of the west top flange in Figure 4.8 reached approximately the same maximum temperature on both days, 28.8°C on the 25th and 29.2°C on the 26th, there was a smaller difference between the temperatures of the top flange and the ambient air on the 26th. The largest difference between the ambient air and the west top flange was 10.9°C and 5.3°C for November 25 and 26, respectively. This smaller magnitude was due to the lower radiation exposure on that day. The girder's sensitivity to direct sunlight is also demonstrated by the way the shape of the temperature curve for the west top flange follows the pyranometer readings and is more jagged on the cloudier day.

Table 4.1 Comparison of Weather Conditions (KATT Weather Station)

	NOVEMBER 25	NOVEMBER 26	DECEMBER 11
7:51 AM	Clear	Scattered Clouds	Clear
8:51 AM	Clear	Mostly Cloudy	Clear
9:51 AM	Clear	Overcast	Clear
10:51 AM	Clear	Overcast	Clear
11:51 AM	Clear	Overcast	Clear
12:51 PM	Clear	Partly Cloudy	Clear
1:51 PM	Clear	Overcast	Clear
2:51 PM	Clear	Scattered Clouds	Clear
3:51 PM	Clear	Scattered Clouds	Clear
4:51 PM	Clear	Partly Cloudy	Clear
5:51 PM	Clear	Clear	Clear
6:51 PM	Clear	Clear	Clear

The temperature measurements at the midpoints of the girder webs during the same two-day time period are shown in Figure 4.9. The lateral gradient plotted against the web temperatures represents the calculated difference between the maximum temperature on one web and the minimum temperature on the other at a given time. During clear days three distinguishable peaks were visible on the lateral gradient curve. The first and third peaks were associated with the sunrise and sunset and were due to one of the webs being exposed to direct solar radiation while the other web was shaded. The middle peak on the gradient curve was connected to the sun coming from behind the building and the western web experiencing direct solar radiation while the eastern web remained in the shade. Figure 4.10 compares the temperature of webs and the flanges. While the temperatures of the members follow each other, the differential shading on the clear day produces larger thermal gradients. This is also shown by the larger magnitudes on the gradient curve in Figure 4.9.

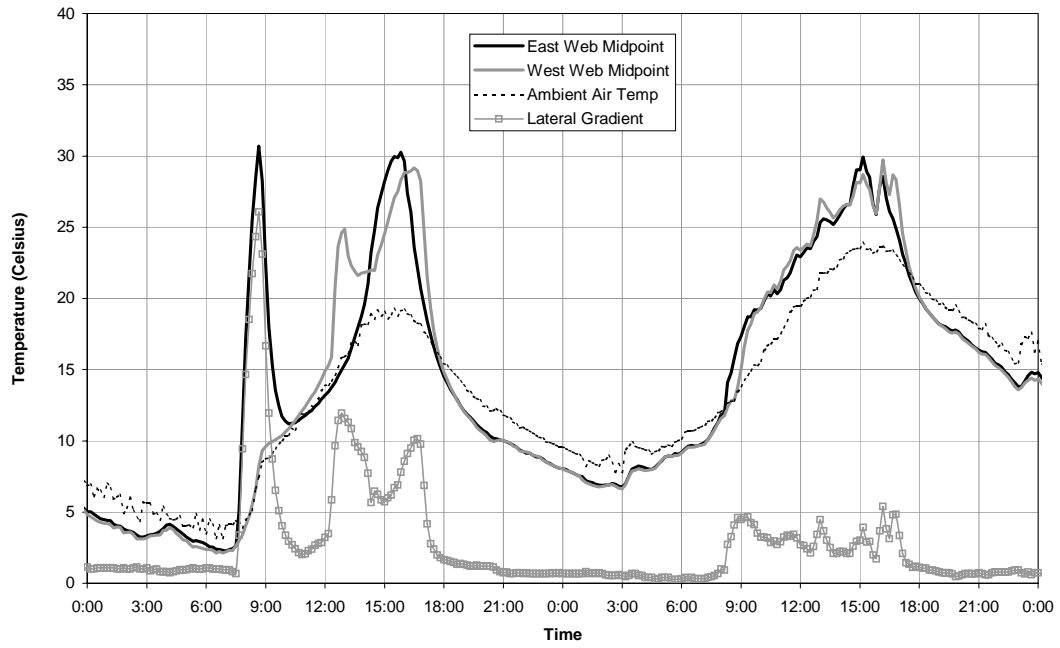


Figure 4.9 Web Temperatures vs. Time (November 25-26 2004)

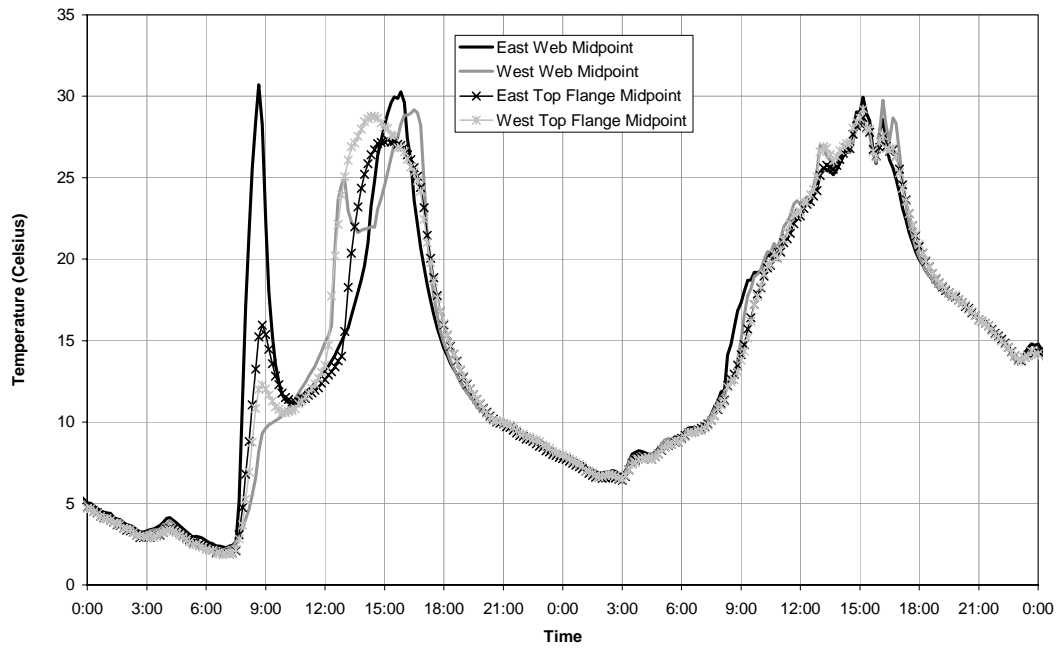


Figure 4.10 Comparison of Web and Flange Temps vs. Time (Nov 25-26 2004)

Figure 4.11 shows the distribution of temperatures on the cross section at the time the maximum lateral temperature gradient was measured. The maximum value of 26.1°C occurred at 8:40 AM on November 25 when the girder was initially exposed to direct solar radiation before it was shaded by the laboratory building. As with the previous temperature distribution plot in Figure 4.7, temperatures are plotted perpendicular to the thick lines representing the girder members. The benchmark temperature for this plot is 25°C and is represented by the dotted lines parallel to the plate members. The large gradient at this time of day is due to the sun being low on the horizon and the eastern web blocking the sunlight from reaching the lower part of the western web. The difference between the warm temperatures measured at the mid-section of the eastern web and the cool temperatures measured on the lower part of the western web produces the large lateral gradient. The maximum lateral gradient occurred on the second coldest morning of testing. The coolest morning ambient air temperature of the sample was measured on December 15, but the maximum gradient on this day was limited to 20°C because the angle of the sun caused the girder to be shaded shortly after sunrise. Cold clear mornings can therefore produce large thermal gradients.

The photograph included with Figure 4.11 was taken twelve days before the maximum lateral gradient was measured at nine o'clock. Since the photograph was taken about twenty minutes after the time when the large gradients typically occurred, the sun had already begun moving behind the building. A patch of sunlight can still be seen on the part of the bottom flange that extends past the eastern web. Figure 4.12 shows a photograph taken at the same time of day that better captures the last part of the morning sunlight hitting the eastern web.

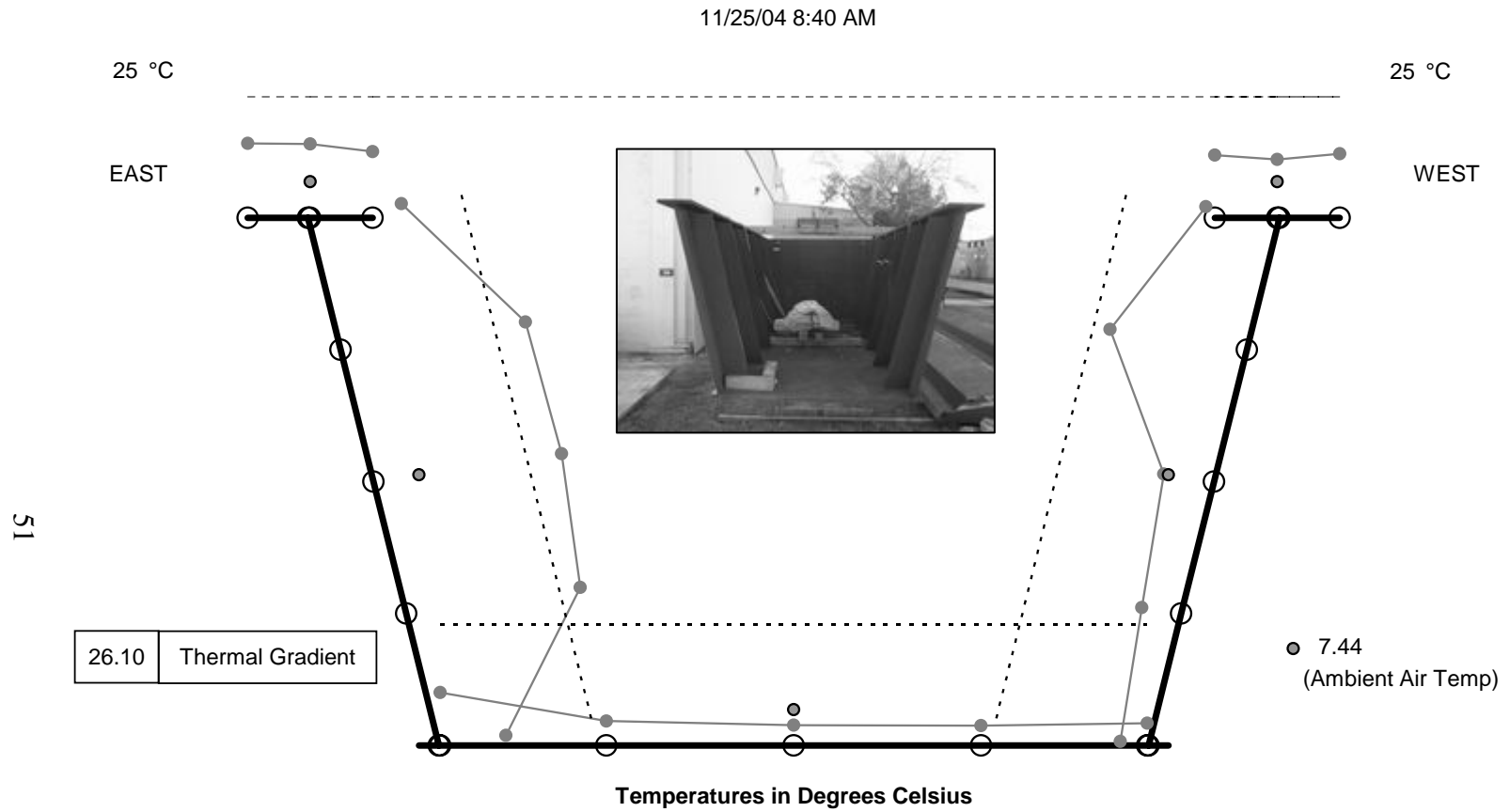


Figure 4.11 Girder Cross Section at Maximum Lateral Temperature Gradient



Figure 4.12 Photograph of Morning Sunlight Hitting Eastern Web

4.5 TEMPERATURE VARIATION ALONG GIRDER

In addition to the temperature at a single cross-section, the variation of temperatures along the girder was needed to properly input data into the finite element thermal prediction model. On December 7, the infrared sensor used to determine the emissivity of the small weathered plates, was also used to make these measurements. The temperature measurements were taken at six cross sections that were about 1, 5, 13, 23, 33, and 53 ft. from the north end of the 54-ft. long tub girder. The section 5 ft. from the north end corresponded to the cross section of the girder that was monitored by thermocouples. At each of the six cross sections that were monitored, six temperature measurements were made, three on each web. The three locations corresponded to the approximate locations of the thermocouples on the webs at the section on the northern end. These

locations are described in this report as the quarter points along the height of the web. Measurements were taken at seven thirty in the morning and every hour after eight o'clock. Figure 4.13 shows the solar radiation, ambient air temperatures, and west top flange temperatures throughout the day. The symbols on the radiation curve represent the times when the temperatures on the six cross sections were measured. The KATT weather station described the entire day as clear and as having a sunrise and sunset at 7:14 AM and 5:30 PM (WU 2005).

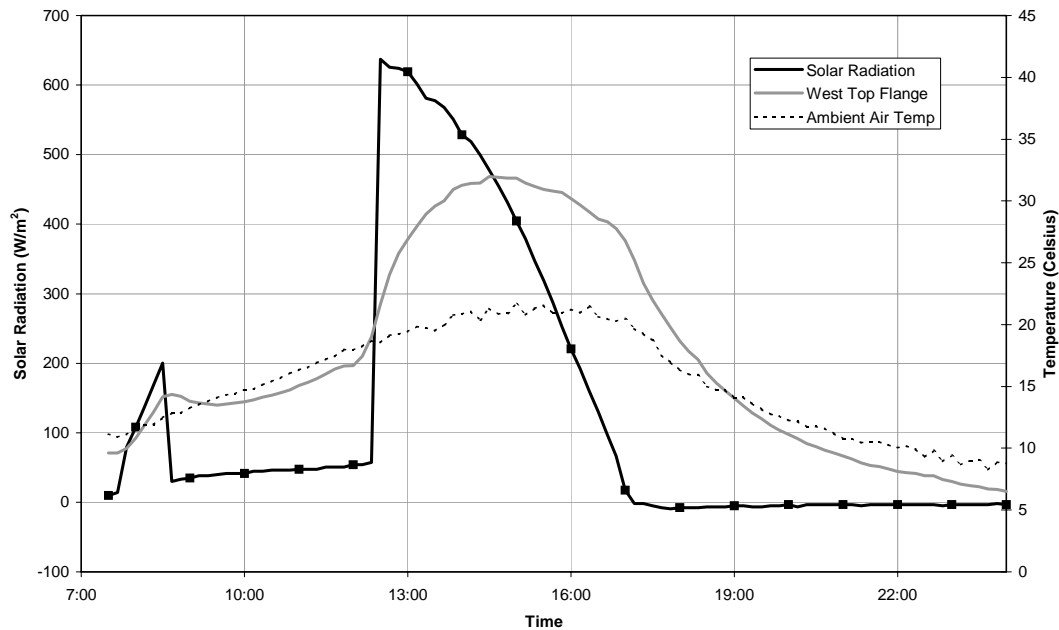


Figure 4.13 Solar Radiation and Temp vs. Time (December 7 2004)

Figure 4.14 and Figure 4.15 show the distribution of the temperatures measured on the west and east web top quarter points, respectively, for different times throughout the day. The distributions along the length of the girder for all six locations generally followed those in Figure 4.14 from seven thirty in the morning until noon. Some differences were apparent, however, due the exposure to the sun of the points 1 and 5 ft. from the northern end in the early morning. This effect ranged from being negligible at the west bottom quarter point to being

significant for the east middle quarter point. At one o'clock in the afternoon, the quarter points on the east side of the girder showed relatively constant distributions, while the west side quarter points began to show varying temperature distributions as in Figure 4.14. A common characteristic of the western response at this time was a spike of warmer temperature at 5 ft. and a dip of cooler temperature at 13 ft. At two o'clock in the afternoon the distributions at all heights were characterized by an increase in temperature from 5 to 13 ft. and a temperature of about 30°C at 53 ft.

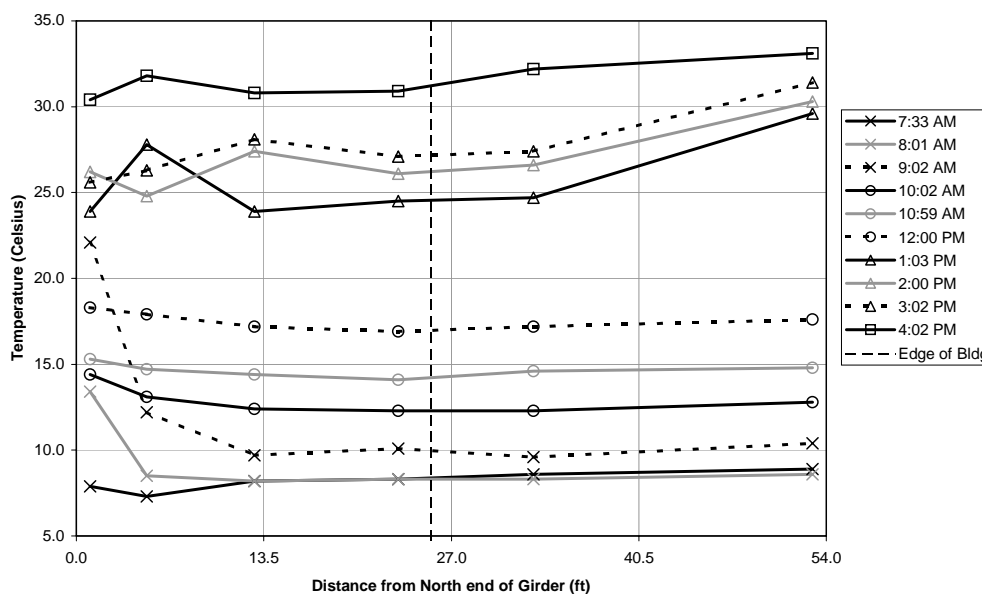


Figure 4.14 Temp vs. Length – Heating of West Web, Top 1/4 Pt. (Dec 7 2004)

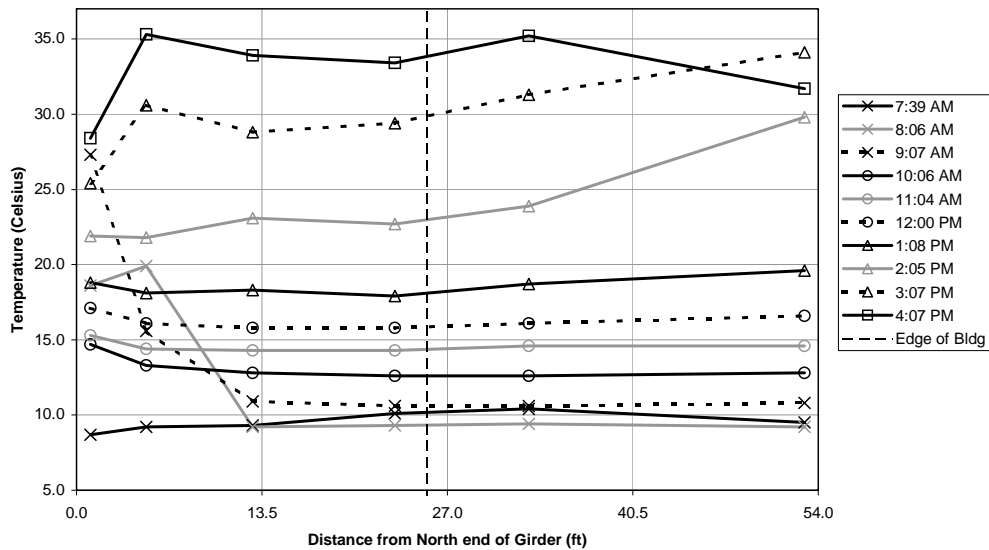


Figure 4.15 Temp vs. Length – Heating of East Web, Top 1/4 Pt. (Dec 7 2004)

Although the temperature distributions varied significantly for the six locations during the late afternoon, a notable feature was a consistent temperature measurement at 53 ft., independent of the time in the afternoon. This clustering of measurements is shown in Figure 4.16 and Figure 4.17 and could be due to the reflected radiation off the building exterior. At 5 ft from the northern end, the difference between the temperature measurements of the infrared sensor and the thermocouples was within $\pm 2.7^{\circ}\text{C}$. Since the most extreme gradients occurred in the morning and in the early afternoon, the lateral and vertical gradients along the girder are shown in Figure 4.18. The comparison of the values from the infrared sensor and the thermocouples in Table 4.2 shows a relatively good correlation except for the lateral gradient at 9 AM.

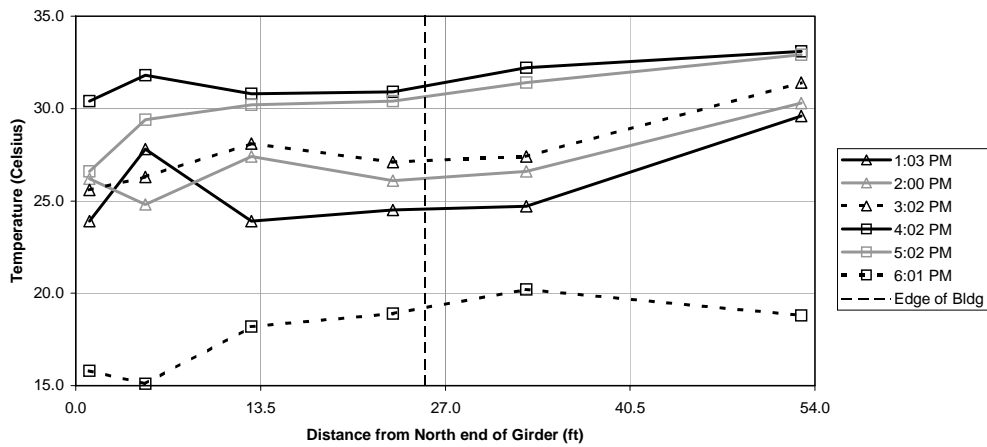


Figure 4.16 Temp vs. Girder Length – West Web – Afternoon (Dec 7 2004)

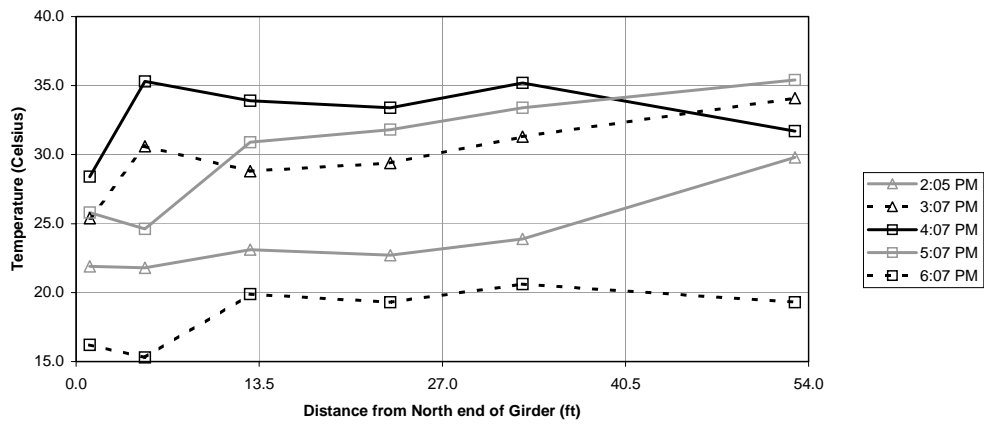


Figure 4.17 Temp vs. Girder Length – East Web – Afternoon (Dec 7 2004)

Table 4.2 Comparison of Temperature Gradients Measurements

	Vertical Gradient	Lateral Gradient
9 AM – Thermocouple	4.8 °C	6.7 °C
9 AM – Infrared Sensor	4.6 °C	4.9 °C
1 PM – Thermocouple	9.3 °C	10.6 °C
1 PM – Infrared Sensor	9.7 °C	10.1 °C

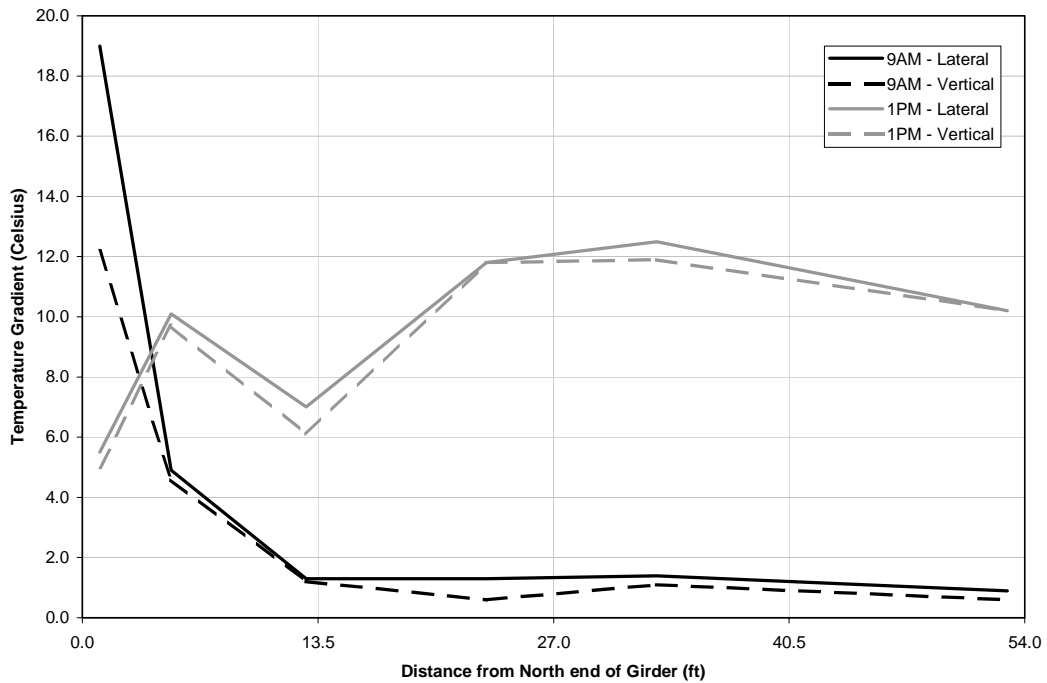


Figure 4.18 Vertical & Lateral Temp Gradients along Girder (Dec 7 2004)

4.6 CONCLUSIONS

Monitoring the temperatures along a cross section of a full size girder demonstrated that the girder reacts quickly to the onset of direct solar radiation, although not as dramatically as the smaller steel plates. The largest thermal gradients on the girder were produced at the onset of direct solar radiation. This occurred in the morning shortly after sunrise and in the afternoon when the girder was no longer shaded by the laboratory building.

For a German project site, Transrapid International specified that the guideway must be designed to accommodate the top flange being between 15 K (15°C) cooler and 25 K (25°C) warmer than the bottom flange (TRI 2000). The design lateral temperature gradient was specified to be ± 15 K (15°C) at the same site. The maximum vertical gradient of 12.5°C measured on December 11 for a

weathered tub girder would comply with these standards, but the maximum lateral gradient of 26.1°C measured on November 25 would not. The most extreme lateral gradients in this test occurred on cold clear mornings shortly after sunrise. If the laboratory did not block the sun in the morning, even larger lateral gradients would have been measured. However, the gradients in this report were calculated using the temperature at two distinct points, while curvatures would typically be computed using the difference between the average uniform temperatures of two girder components. Using average values would therefore produce lower magnitude gradients.

The temperature variation along the length of the girder helped further emphasize the effect of shading. Further tests should be performed to determine the effect of the reflected solar radiation off the side of the laboratory building in the afternoon. The measurements described in this chapter could be compared to predictions made using a finite element model of the girder.

CHAPTER 5

Flat Plate Temperature Predictions

5.1 INTRODUCTION

The overall goal of this project is to predict the temperature gradients experienced by a weathered guideway in order to calculate the resulting temperature deflections. The experimental data for the 100 in² weathered plate described in Chapter 3 and the weathered tub girder in Chapter 4 will be used to determine the accuracy of the predictions. Making the predictions for the flat plate involves using heat transfer concepts along with the ambient air temperature, solar radiation, and wind speed data over a given time. This chapter will discuss the methods used to predict the temperatures of the plate and comment on whether one-hour interval data from a weather station is sufficient to yield accurate results.

5.2 TEMPERATURE CHANGE OVER TIME

Heat transfer concepts involving the convection and thermal radiation modes were used to predict the temperature of the flat plate. Conduction to the wood plate stand supporting the plate was ignored. An equation similar to the one used in Chapter 3 to calculate convection coefficients is used here to calculate the change in temperature over a given time step. A term accounting for the absorption of solar radiation was added to Equation 3.1 to get Equation 5.1.

$$\frac{dT}{dt} = \frac{-1}{m \cdot c} \cdot \left[\varepsilon \cdot \sigma \cdot A_1 (T_{0_i}^4 - T_{\infty_i}^4) + h \cdot A_1 \cdot (T_{0_i} - T_{\infty_i}) - \alpha \cdot A_2 \cdot G_{s_i} \right] \quad (\text{Equation 5.1})$$

where

$$m = \text{mass} = 8.03 \text{ kg}$$

$$c = \text{specific heat for steel} = 480 \text{ J / (kg} \cdot \text{K)}$$

$$\varepsilon = \text{emissivity} = 0.90 \text{ [unitless]}$$

$$\sigma = \text{Stefan – Boltzmann's constant} = 5.67 \cdot 10^{-8} \text{ W / (m}^2 \cdot \text{K}^4)$$

$$A_1 = \text{uninsulated surface area of plate} = 2 \cdot A_2 = 0.129 \text{ m}^2$$

$$T_{0_i} = \text{temperature of the plate at time } i \text{ [K]}$$

$$T_{\infty_i} = \text{temperature of the ambient air at time } i \text{ [K]}$$

$$h = \text{convection coefficient [W / (m}^2 \cdot \text{K)]}$$

$$\alpha = \text{absorptivity} = 0.88 \text{ [unitless]}$$

$$A_2 = \text{surface area of the plate exposed to radiation} = 0.0645 \text{ m}^2$$

$$G_{s_i} = \text{solar radiation at time } i \text{ [W / m}^2]$$

The mass, surface area, emissivity, and absorptivity values for the weathered plate were taken from the experimental results of this project. Neither of the surface areas, A_1 nor A_2 , includes the side surfaces of the flat plate because they were assumed to be insulated by the surrounding wood of the plate stand. The values for Stefan-Boltzmann's constant and the specific heat of steel were taken from a heat transfer text (Incropera & DeWitt 2002). To effectively account for the radiation emitted by the atmosphere, the effective sky temperature should be used. However, the ambient air temperature is used in Equation 5.1 because it is easier to calculate and errors due to this substitution appear to be low during the day. How the difference between the sky and ambient air temperatures was accounted for at night will be described in Section 5.4.1.

5.3 PREDICTION METHODS

The methods used on this project to predict the temperature of the weathered plate involve two main parameters: the time step of the weather data collected and the calculation of the convection coefficient. For these predictions,

both a constant coefficient and a varying coefficient based on the wind speed at each time step were used.

5.3.1 Convection Coefficient

Since a great deal of uncertainty is involved in calculating the convection coefficient, it was assumed to be a constant value of $8.0 \text{ W}/(\text{m}^2\cdot\text{K})$. This value was chosen based on the results described in Chapter 3 for a weathered plate exposed to forced convection. Additional predictions were based on a convection coefficient that was calculated using the wind velocity at each time step. This calculation was made based on the concepts in a heat transfer text for a flat plate experiencing forced convection (Incropera & DeWitt 2002). In addition to the wind velocity, air properties including the kinematic viscosity, thermal conductivity, and the Prandtl number were used to perform this calculation. These air properties were based on a temperature of 300 K and were assumed to be constant throughout the day.

Equations 5.2 through 5.4 were used to compute the convection coefficient. The first step involves using the Reynolds number from Equation 5.2 to determine whether the airflow is laminar or turbulent (Incropera & DeWitt 2002). This airflow distinction determines which equation is used to calculate the average Nusselt number for the entire plate surface. If the Reynolds number is less than 10×10^5 , the flow is considered to be laminar and the Nusselt number is calculated using Equation 5.3 (Hagen 1999). Since turbulent flow was not encountered during the data sample used for these calculations, the corresponding Nusselt equation that combines laminar and turbulent flow is not included here. After the average Nusselt number is calculated it can be used to calculate the average convection coefficient, as shown in Equation 5.4.

$$\text{Re}_{L_i} = \frac{u_{\infty_i} \cdot L}{\nu} \quad (\text{Equation 5.2})$$

$$\overline{Nu}_{L_i} = 0.664 \cdot \text{Re}_{L_i}^{1/2} \cdot \text{Pr}^{1/3} \quad (\text{Equation 5.3})$$

$$\bar{h} = \frac{\overline{Nu}_{L_i} \cdot k}{L} \quad (\text{Equation 5.4})$$

where

Re_{L_i} = Reynolds number, ratio of the inertia and viscous forces at time i [unitless]

u_{∞_i} = wind velocity at time i [m/s]

L = length of the plate = 0.5 m

ν = kinematic viscosity (for air at 300K) = $1.589 \cdot 10^{-5}$ [m²/s]

\overline{Nu}_{L_i} = average Nusselt number, temperature gradient at surface at time i [unitless]

Pr = Prandtl number (for air at 300K) = 0.707 [unitless]

k = thermal conductivity (for air at 300K) = $2.63 \cdot 10^{-2}$ W/(m · K)

\bar{h} = average convection coefficient [W/(m² · K)]

5.3.2 Time Step for Experimental Data

To calculate the temperature predictions for the flat weathered plate and to verify these calculations with measured temperatures, data samples that included plate temperature, solar radiation, wind speed, and ambient air temperature data were required. The dates when this data was available were July 30 - August 3, September 10-13, and September 17-20 2004. The nearby weather stations operated by the Concrete Durability Center (CDC) collected most of the ambient weather information used to make the predictions at an interval of every hour. Although the plate temperature was recorded every ten minutes, using the CDC

data provided the opportunity to determine the accuracy of predictions using one-hour data, which is the typical time interval used by weather stations.

A more refined prediction was possible for the two September data samples because the solar radiation information was gathered from a CM3 pyranometer every ten minutes during those periods. For these samples, the ambient air temperature and wind speed data from the CDC was linearly interpolated to get values every ten minutes. The preliminary predictions for both time intervals involved averaging the ambient conditions at a given time with the previous data point. Figure 5.1 compares the initial prediction results for both the constant and varying convection coefficient methods to the experimental data for July 31. This day produced the lowest absolute error that was calculated using the convection coefficient method. For this day, the preliminary prediction calculations produced a maximum error of 2.4°C for the constant convection method and -3.3°C for the varying convection coefficient method. A positive sign indicates that the prediction overestimated the temperature of the weathered plate, while a negative sign indicates that the temperature of the plate was underestimated. Although only one-hour interval weather information was available for this sample, the less frequent data collection had less of an effect because as Figure 5.3 shows, the solar radiation did not fluctuate often on July 31.

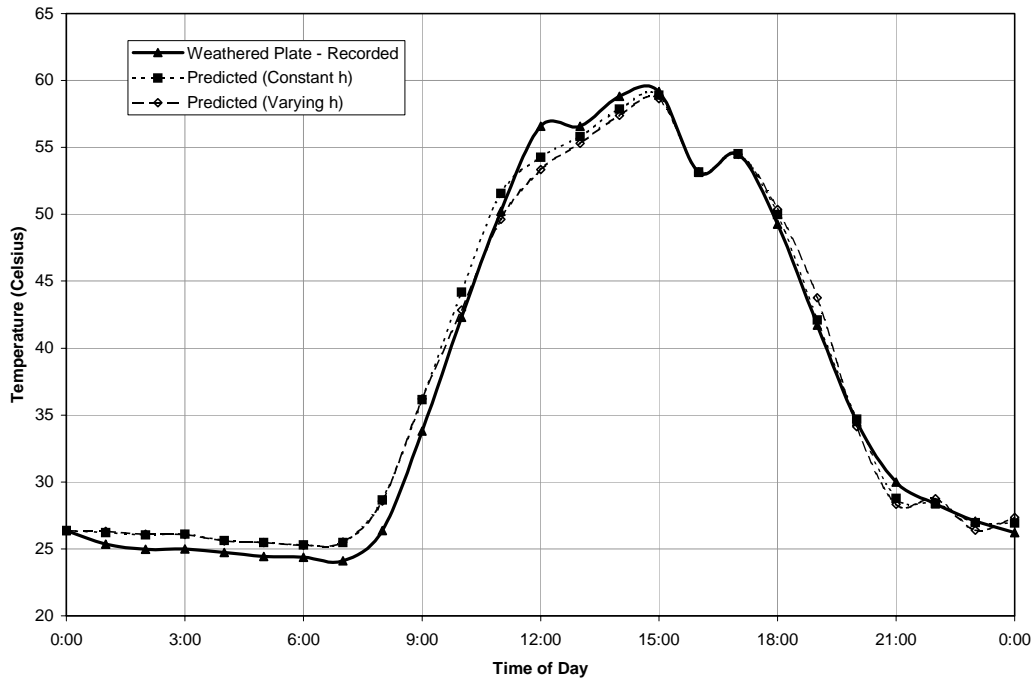


Figure 5.1 Comparison of Prediction Methods (July 31 2004)

Both prediction curves follow the general path of the recorded data fairly well, especially during the second sharp decrease in temperature starting at 3 PM. Figure 5.2 shows in more detail the contribution of each heat transfer mode for the prediction using a constant convection coefficient. The three components of absorbed high frequency radiation, emitted low frequency radiation, and convection, are shown with dotted lines, while the total predicted temperature and the net temperature change at each time step are shown with solid lines. The values at 3 PM are shown to explain how a spreadsheet was used to model the heat transfer with one-hour interval data. These values were calculated using the average of the ambient conditions measured at 2 PM and 3 PM. At 2 PM, the predicted temperature of the plate was 57.87°C. Assuming that each heat transfer component occurred independently for one hour, the change in plate temperature due to convection, emitted radiation, and absorbed radiation would be -23.40°C, -

19.39°C, and 43.81°C, respectively. Summing these values, results in a net increase of 1.02°C, or a predicted temperature of 58.90°C at 3 PM. The weather data used to calculate these predictions is shown in Figure 5.3.

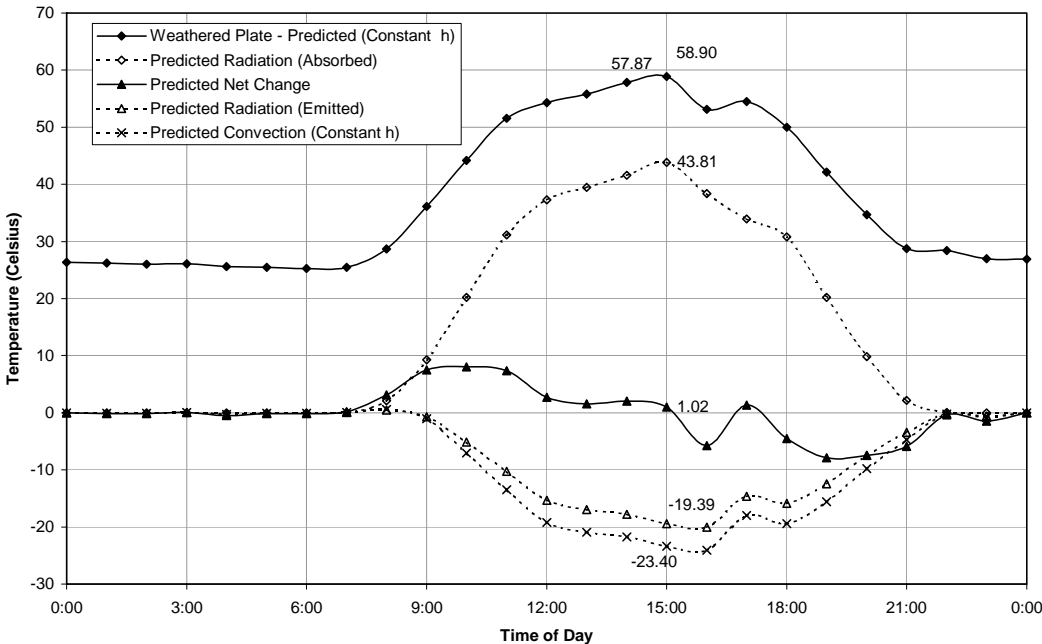


Figure 5.2 Breakdown of Prediction Contributions (July 31 2004)

This figure shows that the predicted temperature curve is dominated by the absorbed radiation curve. A large net change in temperature is therefore generally associated with a sharp increase or decrease in the solar radiation. This connects to the idea discussed in Chapter 4 that the critical times during the day for experiencing a maximum thermal gradient over a girder cross section include the times of the greatest change in the exposure to solar radiation. The largest changes were associated with sunrise, a sudden change in partial shading, and sunset. In addition to showing that the absorbed radiation dominates the predicted temperatures during the day, Figure 5.2 and Figure 5.3 show that predicted temperatures converge to the ambient air temperature at night.

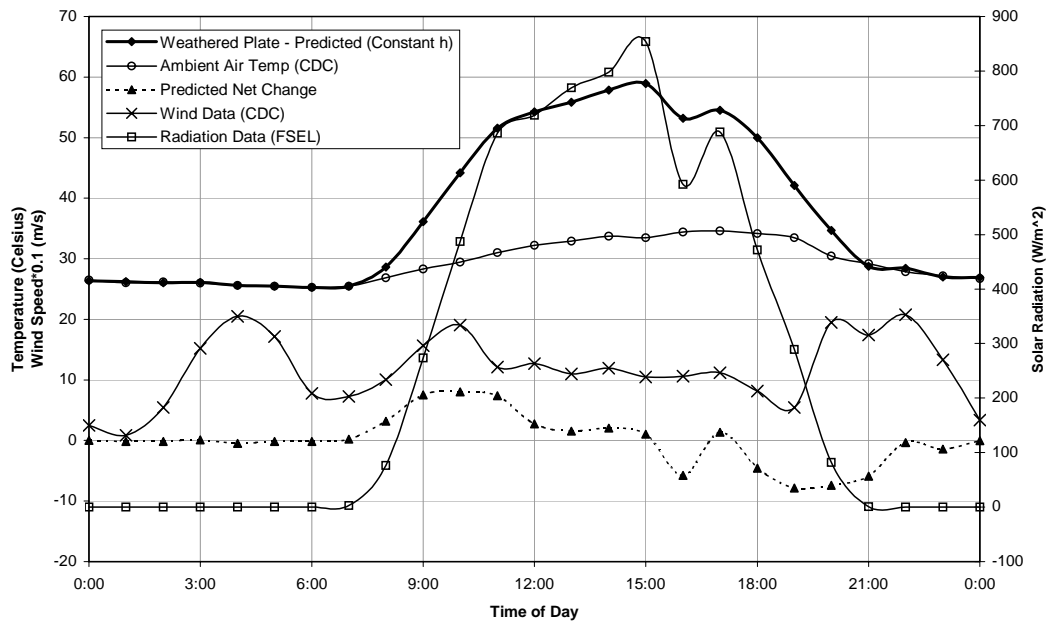


Figure 5.3 Weather Conditions (July 31 2004)

Although the preliminary predictions using the one-hour interval data with a constant convection coefficient yielded relatively accurate temperatures for July 31, Table 5.1 shows that this method produced large errors for other days in the three samples. Calculating the convection coefficient based on the wind speed decreased the errors in most cases, but several days still had maximum errors of about 10°C. Using a more involved heat transfer approach, weather data with a shorter time interval than the typical one-hour readings recorded by weather stations, or both was required to improve prediction accuracy. The maximum errors calculated using the more frequent data recordings gathered during the September data samples are shown in Table 5.2. Although this data produced some improvements, the maximum errors were still relatively large. Note that negative errors represent an underestimation of the temperature.

Table 5.1 Maximum Errors for One-Hour Interval Weather Data

Date	Constant h Error (°C)	Varying h Error (°C)	Date	Constant h Error (°C)	Varying h Error (°C)
July 30	11.0	7.2	Sept 12	9.4	-8.3
July 31	2.4	-3.3	Sept 13	6.9	6.9
Aug 1	6.6	3.3	Sept 17	8.5	8.7
Aug 2	6.1	5.6	Sept 18	7.6	7.1
Aug 3	4.8	5.4	Sept 19	-10.0	-9.5
Sept 10	12.8	11.0	Sept 20	9.6	8.7
Sept 11	14.3	15.1			

Table 5.2 Maximum Errors for Ten-Minute Interval Weather Data

Date	Constant h Error (°C)	Varying h Error (°C)	Date	Constant h Error (°C)	Varying h Error (°C)
Sept 10	11.4	8.8	Sept 17	7.6	8.0
Sept 11	6.2	6.2	Sept 18	-4.2	-6.5
Sept 12	4.8	4.4	Sept 19	8.6	7.7
Sept 13	8.6	7.4	Sept 20	7.3	7.3

5.4 UPDATED PREDICTION METHOD

A C++ computer program was written to produce more accurate results than those produced by the spreadsheet (Kim 2005). In addition to the assumptions made to calculate the preliminary predictions using the spreadsheet, the program interpolated the data to a smaller time step, accounted for the difference between the sky temperature and the ambient air temperature at night, and used an alternative calculation of the convection coefficient. The weather data inputted into the program was linearly interpolated to a time step of six seconds before making heat transfer calculations and ultimately summing the

changes in temperature to produce plate temperatures every ten minutes. The time step at which calculations were performed was adjustable. Ten minutes was chosen for an output to more easily compare to the weathered plate temperature measured at the same frequency.

5.4.1 Effective Sky Temperature

As mentioned in Chapter 3, the measured plate temperatures often reached lower values than the ambient air temperatures at night. This difference results in the error between the predicted and measured temperatures before sunrise in Figure 5.1. The heat loss of the plates correlates to water on the earth's surface freezing when the ambient air temperature is above 0°C on cold clear nights (Incropera and DeWitt 2002). Low values for the radiation emitted by the atmosphere cause this loss.

During the day, the effective sky temperature should be used to model the radiation emitted by the atmosphere, but using the ambient air temperature during this time produces minimal errors. The difference between the temperatures at night is sometimes accounted for by assuming a negative radiation input (Hunt & Cooke 1975). To account for this difference in this report, the ambient air temperature was manually reduced at night by 3°C. This reduction was applied between sunset and sunrise, or 9 PM to 7 AM for the July 30 – August 3 sample and 7 PM to 7 AM for the September samples. This aspect of the program eliminated the large errors calculated at the end of each day using the spreadsheet, and enabled predictions to be made for an entire data sample. Using more days in each prediction helped eliminate the effect of the assumed initial conditions.

5.4.2 Linear Calculation of Convection Coefficient

Predictions using a constant convection coefficient used a value of 8.0 W/(m²*K), the same value used in the spreadsheet. However, predictions using a

varying coefficient incorporated a linear function instead of the flat plate calculations described in Section 5.3.1. The linear function used empirical coefficients, a and b, and had the form of Equation 5.1. The wind speeds are represented by u in m/s. A linear fit of the larger wind speeds experienced during the samples versus the convection coefficients calculated using the flat plate method yielded an equation of $h = 4.5 + 3.3 \cdot u$. This equation was used as an initial approximation because the coefficient for $u = 0$ m/s is $h = 4.5$ W/(m²*K), which is close to the value of 4.6 W/(m²*K) achieved during the natural convection experiment described in Chapter 3. After using this equation for the convection coefficient as an initial guess, the slope coefficient, a, was changed for each data sample until the most accurate results were achieved. The maximum temperature errors using the C++ program are shown in Table 5.3. For varying convection coefficient results, the values of a and b are also included in the table. The weather conditions during the samples are included in the Appendix.

$$h = b + a \cdot u \quad \text{(Equation 5.1)}$$

Table 5.3 Maximum Errors from Predictions Using Program

Date	One-Hour Interval Results (°C)		Ten- Minute Interval Results (°C)	
	Constant h	Varying h (a = 4.6, b = 4.5)	Constant h	Varying h
July 30	9.8	6.5	-	-
July 31	8.3	-7.8	-	-
Aug 1	10.0	-5.6	-	-
Aug 2	9.5	7.7	-	-
Aug 3	8.8	-7.2	-	-
				(a = 5.8, b = 4.5)
Sept 10	10.8	-	11.3	5.0
Sept 11	12.2	-	5.7	-5.0
Sept 12	14.8	-	5.2	-3.6
Sept 13	8.2	-	8.9	4.3
				(a = 3.8, b = 4.5)
Sept 17	12.6	-	7.5	7.0
Sept 18	9.3	-	4.2	-7.0
Sept 19	-7.0	-	8.0	6.7
Sept 20	9.4	-	7.7	6.9

5.5 RESULTS AND CONCLUSIONS

A comparison of the tables in this chapter shows that using the program with a changing convection coefficient decreases the maximum error experienced during a sample. However, results for a particular day are often less accurate than for the constant coefficient. Table 5.3 shows that in general, using data with a smaller time step with a constant convection coefficient can significantly decrease the prediction errors. Days for which the errors increased with a smaller time step, as on September 10, the change was not significant. However, minimizing the time step for September 11 and 12 resulted in large decreases in error. If the heat transfer method described here is used, using solar radiation data with a smaller time step than one hour would substantially increase the accuracy of the predictions. The comparison of the plots for September 13 in Figure 5.4 also demonstrates this finding. Although the error for this day actually increases from 8.2 to 8.9°C, the ten-minute interval curve follows the shape of the recorded data curve more closely than the one-hour data curve. The weather on this day varied between being clear and partly cloudy.

Apart from decreasing the time step of the input weather data, the findings of these predictions produce few additional recommendations. It was expected that using the weather conditions described by a weather station about five miles south of the tub girder, which are included in the Appendix, would determine the likelihood of accurate predictions. However, this was not the case. Instead the one-hour interval data for constant convection suggests that predicting temperatures on August 2, a moderately clear day, was not significantly easier than predicting the temperatures on July 30, a day of thunderstorms and rain. Table 5.3 shows a maximum error of 9.5°C and 9.8°C for August 2 and July 30, respectively. Findings also showed that plate temperatures were both over and

underestimated during clear periods in the samples. Additionally, a correlation could not be made between times of the largest measured solar radiation and the largest temperature overestimations.

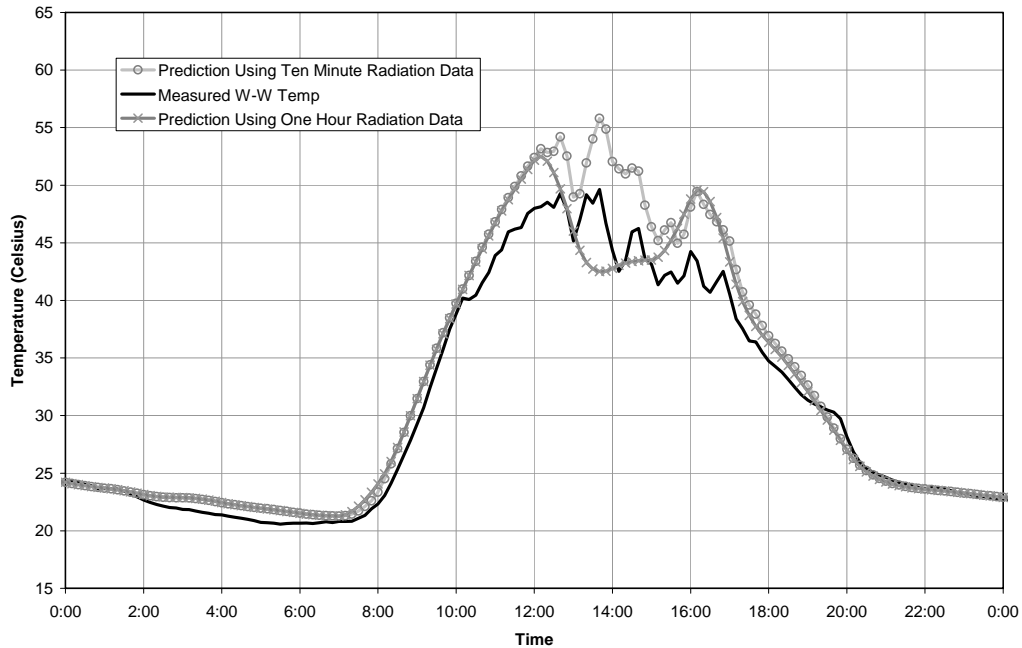


Figure 5.4 Comparison of Predicted & Measured Temps (September 13 2004)

Although simplified heat transfer principles were applied to produce these predictions, it is unclear at this time why using frequent weather readings in close proximity to the experiment setup would produce results with such a large error of $\pm 7.0^{\circ}\text{C}$. Some decrease in accuracy could be due to assumptions made concerning the convective cooling. Although ties to experimental data were used to determine convection coefficients, perhaps more refined tests in an environment with more ideal conditions would yield closer results. Also, assumptions that the sides of the plate were insulated from the wind and that the magnitude of the wind hitting the bottom of the plate was the same as the top of the plate may be incorrect. A gap between the plate sides and the wood plate

stand could negate the assumption of proper insulation, while the wood 2x4s could have prevented wind in the east-west direction from hitting the bottom of the plates, and thus created an inconsistency between the surfaces. Using a finite element program that accounts for additional factors including the shading of the building near the setup of the plates may produce more accurate results than those found in this report.

CHAPTER 6

Conclusions

6.1 TEMPERATURE MEASUREMENTS AND THERMAL GRADIENTS

This report contains the results of temperature monitoring performed on small steel plates with different coatings and a full size weathered girder. The thermal response of the small steel plates showed that weathered steel surfaces behave similarly to a blackbody. Measurements along the cross section of the full size girder demonstrated that the girder responds quickly to an increase or decrease in direct solar radiation.

The largest thermal gradients experienced by the girder during this testing were recorded following a sudden increase in exposure to radiation in conjunction with partial shading. These conditions commonly occurred shortly after sunrise and in the early afternoon. The maximum vertical gradient of 12.5°C experienced during these periods of the day would have satisfied the specification for a project site in Germany that the design must allow for the top flange to be between 15°C cooler and 25°C warmer than the bottom flange. Since the girder monitored during this experiment was an open tub girder, the bottom and top flanges experienced similar solar radiation throughout the warmest part of the day. Although the vertical gradient calculated here would have passed the design criteria at another site, a closed girder resulting in shading of the bottom flange could have produced significantly higher results. Temperature related work on bridges indicates that significant gradients are possible during the mid-to-late afternoon during the summer months (Moorty and Roeder 1992). More testing

could be performed on a closed girder during this period to get a better idea of the possible vertical gradients that could be experienced.

The maximum lateral gradient measured on the weathered girder of 26.1°C would not have passed the design requirement of $\pm 15^\circ\text{C}$ for the German site. In addition to the summer months, extreme lateral gradients on bridges are associated with winter months at sunrise. This was confirmed during this project because the large lateral gradients occurred on the colder mornings. Since lateral gradients on this project were controlled in the morning by the sun moving behind a building, even larger measurements could have been possible. The variation of the vertical and lateral gradients experienced along the length of the girder indicates the importance of considering the shading and reflected radiation from objects surrounding the guideway. It also important to note that the gradients in this report were calculated using the temperature at two distinct points on opposite sides of the girder's cross section. Lower magnitude thermal gradients would have been obtained if instead the differences between the average uniform temperatures of two girder components were used.

Inconclusive results were obtained for the prediction aspect of this report. Errors between the calculated and the measured temperatures could be limited to $\pm 8^\circ\text{C}$, but this range of 16°C makes up 40% of the allowable gradient for the German site example. Further work should be done to determine the effect of the direction of the wind on the plate surface and to explore additional ways of computing an appropriate convection coefficient. Also, developing a method to convert the solar radiation measurements recorded by the CM3 pyranometer used on this project into the direct and diffuse radiation components may also increase the accuracy of the predictions. The methods described here would need to be analyzed further before they could be used to compare with measured data and to

make predictions for potential project sites using available meteorological records.

6.2 IMPLEMENTATION OF MAGLEV TECHNOLOGY

Implementing a Maglev system in the United States could provide a faster travel alternative than what is currently available for ground transportation over moderate distances. If weathering steel is used to control maintenance costs for the guideway, temperature induced deflections need to be accounted for. The temperature measurements and weathered steel surface properties described in this report are intended to provide some of the information needed to predict temperature related deflections for a guideway constructed of weathering steel using a finite element program. Determining the temperature gradients and the resulting deflections a guideway may experience is part of the research required to design a guideway that could be tested in the German test track and perhaps constructed in the future for use in the United States.

Appendix

	9-Jul	10-Jul	11-Jul	12-Jul	16-Jul
Max Air Temp (°C)	32.8	31.3	31.7	32.4	33.6
Min Air Temp (°C)	24.2	21.8	22.7	22.6	24.8
Avg Wind Speed (m/s)	2.4	1.9	1.4	2.2	1.5
Max Sol Rad (W/m ²)	1040	803	958	995	899
Time of Max Sol Rad	14:00	12:00	13:00	14:00	14:00
Morning Conditions (6AM – 11AM)	SC, MC, O	SC, MC, O	MC, O, PC	O, SC, PC, CLR	CLR
Midday Conditions (11AM – 4PM)	MC, SC, PC	MC, SC, PC	SC, PC, MC, HR, O	CLR, SC, PC	PC, CLR
Evening Conditions (4PM – 9PM)	SC, MC, PC, CLR	CLR	SC, PC, CLR	PC, CLR	CLR
	17-Jul	18-Jul	19-Jul	20-Jul	21-Jul
Max Air Temp (°C)	36.7	32.6	34.3	33.6	33.7
Min Air Temp (°C)	24.1	25.9	21.6	23.2	23.3
Avg Wind Speed (m/s)	1.7	1.7	0.9	1.1	1.3
Max Sol Rad (W/m ²)	888	650	953	799	922
Time of Max Sol Rad	15:00	16:00	14:00	14:00	14:00
Morning Conditions (6AM – 11AM)	CLR	MC, O, CLR	CLR	CLR, PC	PC, SC, MC, O
Midday Conditions (11AM – 4PM)	CLR	CLR	CLR	PC, MC	SC, CLR
Evening Conditions (4PM – 9PM)	CLR	CLR	CLR	CLR	CLR, SC
	22-Jul	23-Jul	24-Jul	25-Jul	26-Jul
Max Air Temp (°C)	33.4	34.8	34.9	33.4	29.2
Min Air Temp (°C)	24.7	23.7	24.1	22.1	20.1
Avg Wind Speed (m/s)	2.3	1.8	1.3	2.1	1.9
Max Sol Rad (W/m ²)	829	905	965	938	930
Time of Max Sol Rad	14:00	12:00	15:00	13:00	13:00
Morning Conditions (6AM – 11AM)	MC, SC	MC, SC, PC, C	O, MC, SC, CLR, PC	MC, PC, CLR	CLR
Midday Conditions (11AM – 4PM)	PC, SC	PC, MC, SC	CLR, MC, PC	CLR, PC, SC, MC	CLR
Evening Conditions (4PM – 9PM)	CLR, T	CLR, PC, T	CLR	T, CLR, LTR, R	CLR

CLR = Clear, SC = Scattered Clouds, MC = Mostly Cloudy, PC = Partly Cloudy, O = Overcast, F = Fog, M = Mist, R = Rain, HR = Heavy Rain, LTR = Light Thunderstorms and Rain, T = Thunderstorm
 - Until November 16, Max Temp, Min Temp, and Wind Speed recorded by CDC Weather Stations
 - After November 16, Max Temp and Min Temp recorded by FSEL
 - Prior to August 6, Solar Radiation recorded by CDC Weather Stations
 - After Sept 7, Solar Radiation recorded on tub girder by FSEL (May be affected by shade due to bldg)
 - Weather Conditions at KATT (<http://www.wunderground.com/> 2005)

	27-Jul	28-Jul	29-Jul	30-Jul	31-Jul
Max Air Temp (°C)	31.8	32.6	33.2	31.2	34.6
Min Air Temp (°C)	20.7	24.1	22.8	22.8	25.3
Avg Wind Speed (m/s)	1.00	1.92	2.30	0.99	1.19
Max Sol Rad (W/m ²)	924	729	860	724	854
Time of Max Sol Rad	15:00	14:00	14:00	16:00	15:00
Morning Conditions (6AM – 11AM)	CLR, PC	O, MC, SC, PC	O, R, SC, PC, MC	O, MC, PC	CLR, MC, SC
Middy Conditions (11AM – 4PM)	CLR, PC	-	PC, SC	MC, PC, LTR, HR, CLR	CLR, SC, MC, PC
Evening Conditions (4PM – 9PM)	CLR	SC, PC, CLR	PC, LTR, TR, T	T, MC, CLR	CLR
	1-Aug	2-Aug	3-Aug	4-Aug	5-Aug
Max Air Temp (°C)	35	35	36	36	37
Min Air Temp (°C)	25	25	26	26	26
Avg Wind Speed (m/s)	0.9	0.8	1.0	1.3	1.2
Max Sol Rad (W/m ²)	838	913	920	901	939
Time of Max Sol Rad	14:00	12:00	14:00	14:00	14:00
Morning Conditions (6AM – 11AM)	CLR	CLR	CLR, PC	CLR	CLR
Middy Conditions (11AM – 4PM)	PC, CLR, SC, MC	CLR, MC, PC	PC, CLR	CLR	CLR
Evening Conditions (4PM – 9PM)	T, PC, MC, CLR	CLR	CLR	CLR	CLR
	6-Aug	7-Aug	8-Aug	9-Aug	10-Aug
Max Air Temp (°C)	32.7	31.9	32.9	32.6	34.5
Min Air Temp (°C)	25.7	23.3	24.2	24.3	24.7
Avg Wind Speed (m/s)	1.6	0.7	1.0	1.1	1.2
Max Sol Rad (W/m ²)	-	-	-	-	-
Time of Max Sol Rad	-	-	-	-	-
Morning Conditions (6AM – 11AM)	CLR, PC	O, MC	O, MC, PC, SC	O, CLR	O, PC, CLR
Middy Conditions (11AM – 4PM)	SC, PC, MC	O, MC, PC, CLR	SC, CLR, PC	CLR, PC, MC	SC, CLR, MC
Evening Conditions (4PM – 9PM)	SC, MC, CLR	CLR, MC, O, SC	CLR, MC, SC	SC, PC, MC, CLR	PC, MC, CLR

CLR = Clear, SC = Scattered Clouds, MC = Mostly Cloudy, PC = Partly Cloudy, O = Overcast, F = Fog, M = Mist, R = Rain, HR = Heavy Rain, LTR = Light Thunderstorms and Rain, T = Thunderstorm
- Until November 16, Max Temp, Min Temp, and Wind Speed recorded by CDC Weather Stations
- After November 16, Max Temp and Min Temp recorded by FSEL
- Prior to August 6, Solar Radiation recorded by CDC Weather Stations
- After Sept 7, Solar Radiation recorded on tub girder by FSEL (May be affected by shade due to bldg)
- Weather Conditions at KATT (<http://www.wunderground.com/> 2005)

	11-Aug	12-Aug	13-Aug	14-Aug	15-Aug
Max Air Temp (°C)	33.8	30.3	30.2	31.1	30.9
Min Air Temp (°C)	23.5	19.3	18.5	19.8	20.7
Avg Wind Speed (m/s)	1.2	2.6	0.8	1.0	1.1
Max Sol Rad (W/m ²)	-	-	-	-	-
Time of Max Sol Rad	-	-	-	-	-
Morning Conditions (6AM – 11AM)	CLR	CLR	CLR	CLR, MC, SC	-
Midday Conditions (11AM – 4PM)	CLR, T, TR, PC	CLR	CLR	CLR, PC, SC	-
Evening Conditions (4PM – 9PM)	T, PC, CLR, MC	CLR	CLR	CLR	-
	16-Aug	17-Aug	18-Aug	19-Aug	20-Aug
Max Air Temp (°C)	31.7	32.3	33.4	34.3	35.4
Min Air Temp (°C)	19.8	20.8	21.8	22.2	20.8
Avg Wind Speed (m/s)	0.8	1.0	1.9	3.9	2.0
Max Sol Rad (W/m ²)	-	-	-	-	-
Time of Max Sol Rad	-	-	-	-	-
Morning Conditions (6AM – 11AM)	-	-	CLR, MC, SC	O, MC, SC	CLR, PC, MC, O, SC
Midday Conditions (11AM – 4PM)	-	CLR	SC, MC, PC, CLR	PC, MC, SC	O, SC, CLR, MC
Evening Conditions (4PM – 9PM)	-	CLR	SC, LR, CLR	MC, PC	CLR, PC
	21-Aug	22-Aug	23-Aug	24-Aug	25-Aug
Max Air Temp (°C)	31.1	29.7	31.8	34.3	34.7
Min Air Temp (°C)	21.7	22.4	24.4	25.2	25.2
Avg Wind Speed (m/s)	1.3	1.3	2.7	3.4	3.4
Max Sol Rad (W/m ²)	-	-	-	-	-
Time of Max Sol Rad	-	-	-	-	-
Morning Conditions (6AM – 11AM)	SC, MC, CLR, PC	MC, SC, PC, O	MC, SC, O, LR	MC, O, SC	MC, SC, O, PC
Midday Conditions (11AM – 4PM)	PC, MC, SC, CLR, TR	MC, CLR, LR, PC	MC, SC, PC	SC, PC	CLR
Evening Conditions (4PM – 9PM)	LTR, R, CLR, SC	CLR, T, LTR	PC, CLR, SC	SC, PC, CLR	CLR

CLR = Clear, SC = Scattered Clouds, MC = Mostly Cloudy, PC = Partly Cloudy, O = Overcast, F = Fog, M = Mist, R = Rain, HR = Heavy Rain, LTR = Light Thunderstorms and Rain, T = Thunderstorm
- Until November 16, Max Temp, Min Temp, and Wind Speed recorded by CDC Weather Stations
- After November 16, Max Temp and Min Temp recorded by FSEL
- Prior to August 6, Solar Radiation recorded by CDC Weather Stations
- After Sept 7, Solar Radiation recorded on tub girder by FSEL (May be affected by shade due to bldg)
- Weather Conditions at KATT (<http://www.wunderground.com/> 2005)

	26-Aug	27-Aug	28-Aug	29-Aug	30-Aug
Max Air Temp (°C)	35.2	33.6	31.4	31.7	32.5
Min Air Temp (°C)	25.6	25.3	24.4	22.8	22.6
Avg Wind Speed (m/s)	3.6	3.1	2.0	1.4	1.3
Max Sol Rad (W/m ²)	-	-	-	-	-
Time of Max Sol Rad	-	-	-	-	-
Morning Conditions (6AM – 11AM)	MC, SC, PC	MC, SC, CLR, PC	SC, MC, PC	CLR	CLR
Middy Conditions (11AM – 4PM)	CLR, PC	CLR, PC	CLR, SC, PC	CLR, SC, MC	CLR, SC
Evening Conditions (4PM – 9PM)	CLR	CLR, SC, PC	CLR, T, MC	SC, CLR	CLR
	10-Sep	11-Sep	12-Sep	13-Sep	17-Sep
Max Air Temp (°C)	32.1	33.7	34.3	32.2	35.3
Min Air Temp (°C)	20.6	23.6	22.4	22.4	24.8
Avg Wind Speed (m/s)	1.2	0.7	0.7	1.0	1.0
Max Sol Rad (W/m ²)	942	934	928	968	932
Time of Max Sol Rad	12:40	13:40	14:30	13:40	13:20
Morning Conditions (6AM – 11AM)	MC, PC	MC, O	CLR, MC	SC, PC, CLR	CLR
Middy Conditions (11AM – 4PM)	CLR, MC, PC	PC, CLR, MC	MC, PC, CLR	CLR, PC, SC	CLR, PC
Evening Conditions (4PM – 9PM)	O, CLR, MC	PC, CLR	SC, MC, CLR	CLR, O, R, SC	PC, MC, SC, CLR
	18-Sep	19-Sep	20-Sep	11-Oct	14-Oct
Max Air Temp (°C)	34.3	33.9	32.3	25.9	20.5
Min Air Temp (°C)	23.0	23.9	20.7	16.0	13.7
Avg Wind Speed (m/s)	1.1	1.0	0.8	1.4	2.4
Max Sol Rad (W/m ²)	958	918	884	-	-
Time of Max Sol Rad	14:40	12:40	13:20	-	-
Morning Conditions (6AM – 11AM)	CLR	O	SC, MC, CLR, O	CLR, MC, O, SC	MC, SC, CLR
Middy Conditions (11AM – 4PM)	CLR, PC, SC, MC	MC, SC, PC, CLR	MC, CLR, PC	MC, SC, PC, CLR	CLR
Evening Conditions (4PM – 9PM)	CLR, MC	CLR	SC, PC, CLR	CLR	CLR

CLR = Clear, SC = Scattered Clouds, MC = Mostly Cloudy, PC = Partly Cloudy, O = Overcast, F = Fog, M = Mist, R = Rain, HR = Heavy Rain, LTR = Light Thunderstorms and Rain, T = Thunderstorm
- Until November 16, Max Temp, Min Temp, and Wind Speed recorded by CDC Weather Stations
- After November 16, Max Temp and Min Temp recorded by FSEL
- Prior to August 6, Solar Radiation recorded by CDC Weather Stations
- After Sept 7, Solar Radiation recorded on tub girder by FSEL (May be affected by shade due to bldg)
- Weather Conditions at KATT (<http://www.wunderground.com/> 2005)

	11-Nov	12-Nov	13-Nov	14-Nov	15-Nov
Max Air Temp (°C)	19.0	10.2	10.6	11.0	19.2
Min Air Temp (°C)	10.0	6.8	9.7	9.9	11.2
Avg Wind Speed (m/s)	2.3	2.2	2.1	2.7	1.4
Max Sol Rad (W/m ²)	-	213	165	84	103
Time of Max Sol Rad	-	13:20	11:10	12:20	12:00
Morning Conditions (6AM – 11AM)	O, PC, CLR	O	O	O, LTR, TR, HTR	R, HTR, LR, O, F
Midday Conditions (11AM – 4PM)	CLR	O	O, LR	R, LR, O	F, O
Evening Conditions (4PM – 9PM)	CLR	O	O	O	O
	16-Nov	24-Nov	25-Nov	26-Nov	27-Nov
Max Air Temp (°C)	21.1	15.6	19.3	23.9	19.5
Min Air Temp (°C)	17.5	6.5	3.1	7.8	7.1
Avg Wind Speed (m/s)	0.9	-	-	-	-
Max Sol Rad (W/m ²)	-	686	655	547	667
Time of Max Sol Rad	-	12:40	12:20	14:40	12:20
Morning Conditions (6AM – 11AM)	LR, O	O, SC, PC, MC	CLR	O, SC, MC	CLR
Midday Conditions (11AM – 4PM)	O, LR, R	CLR	CLR	O, SC, PC	CLR
Evening Conditions (4PM – 9PM)	O, LR	CLR	CLR	PC, CLR	CLR
	28-Nov	7-Dec	8-Dec	11-Dec	12-Dec
Max Air Temp (°C)	23.4	21.6	19.1	22.4	27.5
Min Air Temp (°C)	4.9	-	6.7	7.0	6.6
Avg Wind Speed (m/s)	-	-	-	-	-
Max Sol Rad (W/m ²)	629	637	329	620	605
Time of Max Sol Rad	12:20	12:30	12:40	12:30	12:40
Morning Conditions (6AM – 11AM)	CLR	PC, CLR, SC, O	CLR	CLR	CLR
Midday Conditions (11AM – 4PM)	CLR, PC, SC	O, PC, MC	CLR	CLR	CLR
Evening Conditions (4PM – 9PM)	MC, O	MC, CLR	CLR	CLR	CLR

CLR = Clear, SC = Scattered Clouds, MC = Mostly Cloudy, PC = Partly Cloudy, O = Overcast, F = Fog, M = Mist, R = Rain, HR = Heavy Rain, LTR = Light Thunderstorms and Rain, T = Thunderstorm
- Until November 16, Max Temp, Min Temp, and Wind Speed recorded by CDC Weather Stations
- After November 16, Max Temp and Min Temp recorded by FSEL
- Prior to August 6, Solar Radiation recorded by CDC Weather Stations
- After Sept 7, Solar Radiation recorded on tub girder by FSEL (May be affected by shade due to bldg)
- Weather Conditions at KATT (<http://www.wunderground.com/> 2005)

	13-Dec	14-Dec	15-Dec		
Max Air Temp (°C)	14.7	10.3	13.8		
Min Air Temp (°C)	6.0	0.4	-4.9		
Avg Wind Speed (m/s)	-	-	-		
Max Sol Rad (W/m ²)	620	643	620		
Time of Max Sol Rad	12:40	12:40	12:40		
Morning Conditions (6AM – 11AM)	CLR	CLR	CLR		
Midday Conditions (11AM – 4PM)	CLR	CLR	CLR, PC		
Evening Conditions (4PM – 9PM)	CLR	CLR	CLR, MC, O		

- CLR = Clear, SC = Scattered Clouds, MC = Mostly Cloudy, PC = Partly Cloudy, O = Overcast, F =Fog, M = Mist, R = Rain, HR = Heavy Rain, LTR = Light Thunderstorms and Rain, T = Thunderstorm
- Until November 16, Max Temp, Min Temp, and Wind Speed recorded by CDC Weather Stations
 - After November 16, Max Temp and Min Temp recorded by FSEL
 - Prior to August 6, Solar Radiation recorded by CDC Weather Stations
 - After Sept 7, Solar Radiation recorded on tub girder by FSEL (May be affected by shade due to bldg)
 - Weather Conditions at KATT (<http://www.wunderground.com/> 2005)

REFERENCES

1. Albrecht, P. and A. H. Naeemi. "Performance of Weathering Steel in Bridges." National Cooperative Highway Research Program Report, 169 pp, July 1984.
2. Campbell Scientific, Inc., (CSI). LI200X Pyranometer Instruction Manual. Logan, Utah: Campbell Scientific, Inc., 1997.
3. Campbell Scientific, Inc., (CSI). CM3 Pyranometer Instruction Manual. Logan, Utah: Campbell Scientific, Inc., 2002.
4. Figliola, Richard S. and Donald E. Beasley. Theory and Design for Mechanical Measurements. New York: John Wiley & Sons, Inc., 1995.
5. Giancoli, Douglas C. Physics for Scientists & Engineers. Upper Saddle River, New Jersey: Prentice Hall, 2000.
6. Hagen, Kirk D. Heat Transfer with Applications. Upper Saddle River, New Jersey: Prentice-Hall, Inc., 1999.
7. Henke, Volker and Horst Falkner. "Transrapid – A High Speed Magnetically Levitated Train System." Transrapid International.
8. Hunt, Bruce and Nigel Cooke. "Thermal Calculations for Bridge Design." Journal of the Structural Division, ASCE, V. 101, No. 9, pp. 1763-81, 1975.
9. Incropera, Frank P. and David P. DeWitt. Fundamentals of Heat and Mass Transfer. Hoboken, New Jersey: John Wiley & Sons, Inc., 2002.
10. Kim, Hyeong Jun. Thermal.exe. February 2005.
11. Mangerig, Ingbert, et al. "Thermal effects on guideways for high speed magnetic levitation transportation systems." International Association for Bridge and Structural Engineering (IABSE), 2003.
12. Moorty, Shashi and Charles W. Roeder. "Temperature-Dependent Bridge Movements." Journal of Structural Engineering, ASCE, V. 118, No. 4, pp. 1091-1105, 1992.

13. National Oceanic and Atmospheric Administration (NOAA). "Pressure Altitude." National Weather Service Forecast Office: El Paso Area, 25 Feb. 2005. <<http://www.srh.noaa.gov/elp/wxcalc/pressurealtitude.shtml>>.
14. Ražnjević, Kuzman. Handbook of Thermodynamic Tables. New York: Begell House, Inc., 1995.
15. Transrapid International (TRI). "California Nevada Interstate Maglev Project: Design Loads for Preliminary Girders Type I and Type II in Steel Construction and Guideway Plates Type III in Steel or Concrete Construction." Design Document, 2000.
16. Transrapid International (TRI). "California Nevada Interstate Maglev Project – Transrapid Guideway System: Overview of Styles and Types, Deflection Limits, Tolerances, Offsets." Design Document, 2002.
17. Transrapid International (TRI). "Comparison of System Characteristics." Design Document, 2003.
18. Weather Underground (WU). April 2005. <<http://www.wunderground.com/>>.

VITA

Travis Bertram Richards was born on May 7, 1981 in San Mateo, California, to his parents Michael and Carol Richards. He attended Saint Francis High School in Mountain View, California before beginning his undergraduate work in civil engineering at the University of California, Berkeley. After receiving his Bachelor of Science in May 2003, Travis began work as a Graduate Research Assistant at The University of Texas at Austin in Fall 2003 and completed his Master of Science in Engineering in May 2005.

Permanent Address: 2118 Whipple Avenue
Redwood City, CA 94062

This thesis was typed by the author.